A Census of Early-type Galaxy Disks from the ALMA aRchive (CEDAR)

Nicholas LeVar

A senior thesis submitted to the faculty of
Brigham Young University
in partial fulfillment of the requirements for the degree of

Bachelor of Science

Benjamin Boizelle, Advisor

Department of Physics and Astronomy

Brigham Young University

ABSTRACT

A Census of Early-type Galaxy Disks from the ALMA aRchive (CEDAR)

Nicholas LeVar
Department of Physics and Astronomy, BYU
Bachelor of Science

The Atacama Large Millimeter/sub-millimeter Array (ALMA) archive now contains a wealth of local galaxy observations, offering rich insight into the molecular gas that powers star formation and supermassive black hole (BH) accretion. In some instances, this molecular gas forms a round circumnuclear disk (CND) that spans $\sim$100 pc to several kpc, providing a crucial probe of the inner gravitational potential. To aid in future studies of luminous early-type galaxies (ETGs), I present a Census of ETG Disks from the ALMA aRchive (CEDAR), with targets selected from nearby (z $\lesssim$ 0.05; $D_L \lesssim$ 250 kpc) ETGs whose ALMA carbon monoxide (CO) imaging is sufficiently high angular resolution ($\theta_{FWHM} \lesssim$ 1") to resolve most CNDs. In a select few cases, the ALMA archive contains CO imaging at different angular resolutions, or of separate CO transitions. When possible, we performed self-calibration processes prior to standard imaging to ensure consistency and quality. These imaging products include spectral CO data cubes, moment maps, position-velocity diagrams, integrated velocity profiles, and a variety of continuum images (featuring various weighting methods for both total and resolved continuum images). For this first sample observed in Cycles 2-4, we present molecular gas properties and kinematics together with continuum emission for > 100 ETGs. Typical molecular gas masses in this sample range from 10^6 - 10^{10} $M_\odot$. Nearly three fourths of the sample shows regular gas kinematics with typical circular velocity amplitudes reaching 200-400 km/s. In CNDs that are sufficiently well resolved, a small fraction (10-20) show evidence for CO emission originating from within the BH sphere of influence (SOI). We compare this sample with results from previous ETG surveys, analyze the kinematic behavior of these gas disks, and explore their properties.

Keywords: Early-type Galaxies (429) — Galaxy Circumnuclear Disks (581) — Galaxy nuclei (609) — Galaxy structure (622)

ACKNOWLEDGMENTS

I am eternally grateful for my mom, dad, sibling, friends, and family who have supported me throughout my undergraduate career and helped me through the difficult moments. I want to thank my advisor, Dr. Ben Boizelle, for his mentorship, support, and friendship over the past three years. The work done in this thesis is builds off of previous work by Dr. Boizelle and undergraduate students at BYU such as Joshua Jones, Ben Derieg, Edison Carlisle, and Connor Camacho. I am grateful for the opportunity to extend their work.

Contents

Table of Contents **iv**

List of Tables **v**

List of Figures **v**

1 Introduction **1**

2 Data & Methods **9**
2.1 Sample Selection 9
2.2 ALMA Data Processing 12
2.3 Continuum Products 17
2.4 Emission-line Products 17

3 Results **24**
3.1 Molecular Gas Masses 24
3.2 CND Morphologies 27
3.3 Kinematic Analysis 29

4 Discussion **34**
4.1 Formation of Molecular CNDs 34
4.2 Star Formation in ETGs 35
4.3 Supermassive black holes 36
4.4 Different CO Transitions 40
4.5 Conclusion 41

Bibliography **44**

Index **51**

List of Tables

2.1 CEDAR host galaxy properties 15

2.2 CO Emission Properties 19

4.1 Literature-compiled dynamical black hole masses 39

4.1 Literature-compiled dynamical black hole masses 40

List of Figures

1.1 Hubble Tuning Fork 2

1.2 HST Imaging of Dusty CNDs 4

2.1 Galaxy Properties of CEDAR Sample 11

2.2 CO Moment 0 (Flux) Maps 21

2.3 Moment 1 (Velocity) Maps 22

2.4 Position vs Velocity Diagrams 23

3.1 CO vs Host Galaxy Properties 26

3.2 Comparison of ALMA and CARMA Imaging 29

3.3 CO Kinematic PA for CEDAR galaxies 30

3.4 Kinematic Misalignment Histogram 33

4.1 CEDAR BH properties 38

4.2 R_{32} map of NGC 6861 42

4.3 Thermodynamic Modeling of NGC 6861 43

Chapter 1

Introduction

Galaxies are among the grandest and most distinctive structures in the universe. Composed of billions to hundreds of trillions of stars, these objects are cosmic building blocks and appear in a wide variety of shapes and sizes. Since Edwin Hubble's seminal work (Hubble 1926), galaxies have been broadly grouped into two categories: **early-type** and **late-type**. Early-type galaxies (ETGs) consist of elliptical and lenticular galaxies whereas late-type galaxies (LTGs) include disk galaxies such as the Milky Way. This categorization is based primarily on optical morphology (Figure 1.1): ETGs are dominated by a prominent bulge component, whereas LTGs are disk-dominated. The "early/late" terminology originated from the (now obsolete) idea that ETGs represent an early stage of galaxy formation and LTGs the endpoint; in fact, luminous ETGs are now understood to be a late stage of galaxy evolution.

ETGs span an enormous mass range; from modest galaxies of $\sim 10^8$ $M_\odot$ to massive $\sim 10^{14} M_\odot$ central dominant (cD) galaxies that reside in the centers of galaxy clusters. Their physical sizes are equally diverse, with diameters from $\sim$1 kpc to $\sim$1 Mpc. By comparison, LTGs typically have masses of 10^9-10^{12} $M_\odot$ and diameters of 5-100 kpc, so ETGs occupy a broad region of galaxy-property parameter space. ETGs also tend to be much redder than their late-type counterparts,

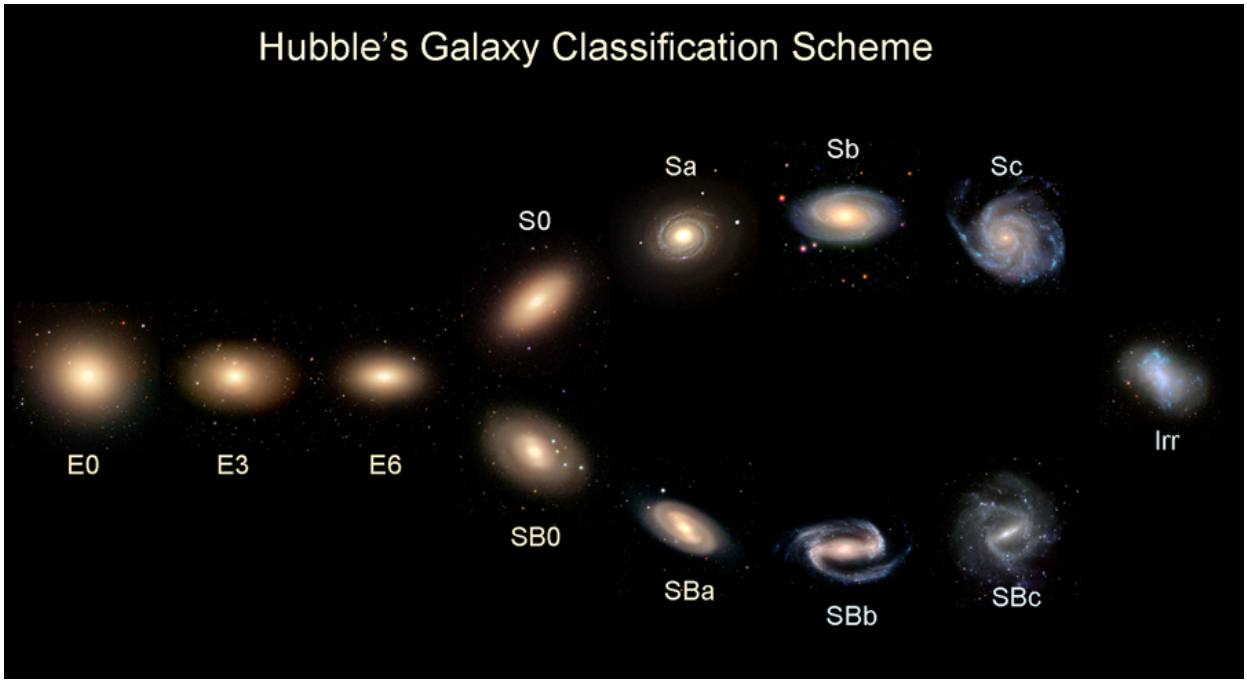

Figure 1.1 Hubble's "Tuning Fork" including (left to right) elliptical (E), lenticular (S0), spiral (Sa-c) and barred spiral (SBa-c), and irregular galaxies (Irr). Image taken from CANDELS (Grogin et al. 2011).

indicating lower specific star-formation rates, older stellar populations, and different interstellar medium (ISM) characteristics.

A coherent picture of galaxy evolution must include a detailed understanding of the ISM. In a given galaxy, the ISM is usually divided into three phases that differ by more than six orders of magnitude in temperature and density: the **hot ionized medium**, the **warm medium**, and the **cold medium**. Although the cold ISM (dust plus molecular and atomic gas) accounts only for a fraction of a galaxy's total baryonic mass – roughly 10-20% for star-forming LTGs, and $\lesssim 3\%$ in ETGs (Saintonge & Catinella 2022)– it is typically is the dominant ISM phase by mass. Cold molecular gas, with typical temperatures of $\sim$ 10-100 K and densities of $\sim 10^3$-10^6 cm^{-3}, is mostly molecular hydrogen (H_2), but also contains hundreds of other molecules; more than 200 of which have been detected in the Milky Way's ISM (McGuire 2018). Because H_2 is a perfectly symmetric molecule,

it radiates only through quadrupole transitions with excitation energies > 500 K, conditions rarely met in molecular clouds. Accordingly, molecular gas is usually traced by its second-most-abundant molecule, carbon monoxide (CO).

Cold ISM is directly involved in many aspects of galaxy evolution and encodes information on both small and large scales. Molecular gas fuels star formation because its density and low temperature allow it to collapse into star-forming regions. Circumnuclear cold gas is also thought to feed active galactic nuclei (AGN), and may play a key role in the coevolution of supermassive black holes (SMBHs) and their host galaxies; a link suggested by the tight correlations between SMBH mass and various host properties (Ferrarese & Merritt 2000; Gebhardt et al. 2000; Kormendy & Ho 2013).

Historically, ETGs were labeled "red and dead," presumed to have negligible gas and dust and, therefore, minimal star formation (de Vaucouleurs 1959; Kennicutt 1998; Sandage 1961). Early CO studies (e.g. Johnson & Gottesman 1979) appeared to confirm the absence of substantial molecular gas reservoirs, although the limiting masses were not very constraining. Over the few decades, however, high-quality imaging and spectroscopy have complicated this view. Far-infrared surveys have revealed moderate amounts of cold thermal dust ($T_{\rm dust} \sim 20-40$ K) in $\sim$20$-$25% of ellipticals and half of lenticulars (di Serego Alighieri et al. 2013; Knapp et al. 1989; Kokusho et al. 2019; Smith et al. 2012). Many such dusty regions have been resolved by the *Hubble Space Telescope* (HST) into dusty filaments and morphologically regular circumnuclear disks (CNDs) with radii of a few $\times 10^2$ pc to a few kpc (Lauer et al. 2005; Tran et al. 2001), as shown in Figure 1.2. Single-dish CO observations detected a fraction of these CNDs–primarily in lenticulars–while placing limits of several $\times 10^8$ $M_\odot$ (e.g., Braine et al. 1997; Knapp & Rupen 1996; Sage & Wrobel 1989; Wiklind & Henkel 1989) to just a few $\times 10^7$ $M_\odot$ (Young et al. 2011). More sensitive interferometric observations have since resolved disk-like behavior and pushed detection limits down to the few $\times 10^6$ $M_\odot$ to 10^7 $M_\odot$ (e.g., Alatalo et al. 2013; Boizelle et al. 2017; Ruffa et al. 2019). Taken all

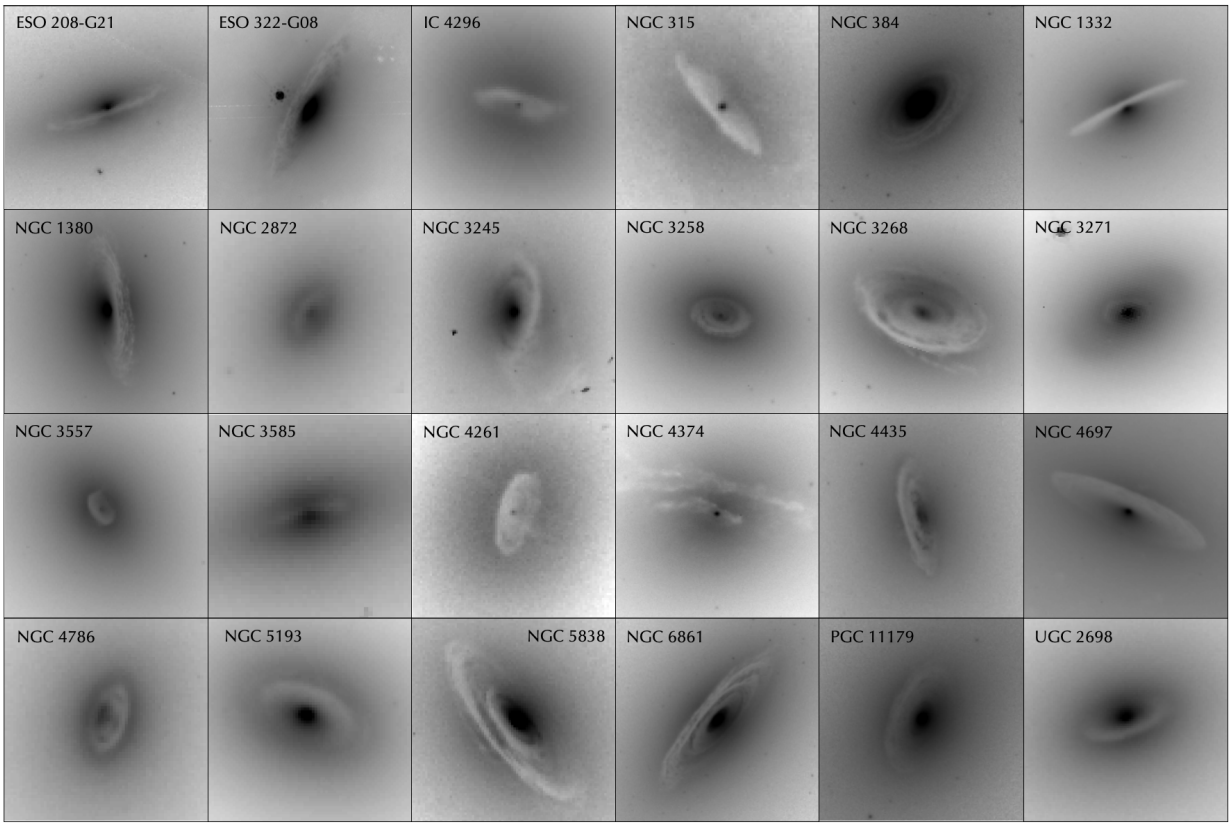

Figure 1.2 Dusty CNDs in ETGs as see in HST imaging

together, $\sim$30% of ETGs host significant atomic-gas reservoirs (di Serego Alighieri et al. 2007; Serra et al. 2012) and $\gtrsim$20% contain detectable molecular gas (Young et al. 2011); $\sim$10% exhibit morphologically regular dusty CNDs (Lauer et al. 2005; Tran et al. 2001).

Large imaging surveys such as especially the Sloan Digital Sky Survey (SDSS; York et al. 2000) have demonstrated a bimodality in the color and mass distribution of galaxies in the local universe ($z \lesssim 0.1$; e.g., Baldry et al. 2006; 2004; Bamford et al. 2009). The massive ETGs of the red sequence likely formed at high redshift from major mergers of star-forming LTGs, triggering starburst that exhausted their gas and left them quiescent. Yet up to $\sim$30% of ETGs are bluer, signaling ongoing or recent star formation (Schawinski et al. 2007a;b). Far-UV and mid to far-IR data provide some

support for this activity, though contamination or alternative sources may mimic the signatures (Davis et al. 2014).

The origin, evolution, and longevity of dusty CNDs remain debated. Increasing physical resolution has demonstrated close agreement between gas and host galaxy kinematic/photometric axes with a few outliers (Davis et al. 2017), although the highest resolution imaging suggests more complex disk warping, typically at the few-degree level (Boizelle et al. 2017; Ruffa et al. 2019). Approximately flat, dynamically cold disks (ratio of ordered to dispersive emission-line motion $v/\sigma \gg 1$) show slight warping and asymmetrical streamers that suggest either: an ongoing process of settling into the galaxy midplane (e.g., Tran et al. 2001) that may take a few $\times$100 Myr to >Gyr (Davis & Bureau 2016; van de Voort et al. 2015); or, evidence for a non-axisymmetric potential (e.g., Habe & Ikeuchi 1988). Cases with higher gas disk misalignment are consistent with an external origin while the majority can also be explained by *in situ* stellar evolution and feedback processes (Babyk et al. 2019; Davis et al. 2017; Lagos et al. 2014).

Star formation in ETGs is still poorly understood, in part due to the difficulty in resolving clumpy disk emission for even relatively local cases ($\lesssim$20 Mpc). For ETGs, cold molecular gas typically dominates the ISM mass budget while accounting for a small fraction of the total baryonic mass ($\lesssim$3% for ETGs compared to 10$-$20% for LTGs; Saintonge & Catinella 2022). Given molecular gas in ETGs is typically very centrally concentrated (typical outer dusty radius $R_{\rm dust}/R_e \sim 0.1-0.5$ relative to the host galaxy half-light radius R_e; e.g., Davidson et al. 2024), the estimated SF rates of $0.1-1\ M_\odot\ {\rm yr}^{-1}$ (Kennicutt 1998) result in SF surface mass densities that are comparable to those for normal star-forming LTGs. However, estimated and simulated SF efficiencies in ETGs appear systematically lower than expectations from measured gas surface mass densities (Davis et al. 2014; Jiang et al. 2022). During the formation of massive ETGs, the growth of the central gravitational potential should stabilize a CND against fragmentation and collapse to create stars, morphologically quenching SF (Martig et al. 2009; 2013). Some lower SF may remain due to local overdensities

or cloud collisions. At present, though, there remains significant uncertainty in the SF rate due to: moderate-to-high dust obscuration ($A_V \sim 1-5$ mag; e.g., Boizelle et al. 2019; Davidson et al. 2024); optical/UV continuum or emission-line contamination by active nuclei, which is difficult to disentangle given $R_{\rm dust} \sim 0\farcs2 - 1''$ for many local ETGs; and mid-to-far-IR SF tracers having insufficient resolution to clearly rule out diffuse dust grains being heated by interstellar radiation instead of SF.

Some of this circumnuclear cold gas is thought to fuel low-luminosity active galactic nuclei (AGN; Izumi et al. 2016), which at times are just barely detected in mm-to-radio wavelength imaging at sub-mJy levels. More extreme AGN feedback has been connected to SF regulation during episodic gas accretion or merger events, playing a significant role in the correlation of supermassive black hole (BH) masses ($M_{\rm BH}$) and various host galaxy properties (including stellar velocity dispersion $\sigma_\star$ and bulge luminosity L_K; Ferrarese & Merritt 2000; Gebhardt et al. 2000; Kormendy & Ho 2013), suggesting coevolution over cosmic time. The detailed picture remains poorly understood, including how this coevolution depends on environment and the core vs. cusp dichotomy.

The Atacama Large Millimeter/submillimeter Array (ALMA) offers an order-of-magnitude improvement in sensitivity and both angular and spectral resolution over the previous generation of mm/sub-mm facilities. In addition to several high redshift galaxy continuum and line programs (e.g., Franco et al. 2018; Fujimoto et al. 2023; Le Fèvre et al. 2020; Walter et al. 2016), there are several ongoing ALMA CO (and dense-gas) surveys of local radio galaxies (Ruffa et al. 2019), central galaxies in clusters (e.g., Ganguly et al. 2023; Olivares et al. 2019), active galaxies (Izumi et al. 2013; 2015), and LTGs (Leroy et al. 2021; 2022) that seek to resolve thermal dust and molecular gas kinematic properties, line excitation, and AGN fueling in unprecedented detail. ALMA CO has also been used to map out CND rotation within the BH sphere of influence (SOI), allowing for high-quality $M_{\rm BH}$ determination for an ever-growing sample of both ETGs (e.g., Barth et al.

2016a;b; Boizelle et al. 2019; 2021; Cohn et al. 2021; Davis et al. 2017; 2018; Kabasares et al. 2022; North et al. 2019; Ruffa et al. 2023; Smith et al. 2019) and LTGs (e.g., Nguyen et al. 2020). The PHANGS–ALMA survey of $\sim$100 nearby LTGs (with luminosity distance $D_L < 20$ Mpc) has mapped out molecular gas and dust properties in normal SF galaxies (Baron et al. 2024; Leroy et al. 2021; 2022). Unfortunately, no commensurate survey of gas and dust in ETGs has been pursued with ALMA. Smaller surveys using different approaches have highlighted a range of properties, including different CO surface brightness behaviors and excitation, disk warping, rotation curves, non-circular motion, alignment with jet axes, and the dust-to-gas mass ratio (e.g., Boizelle et al. 2017; Ruffa et al. 2019).

Here, I present a Census of Early-type Galaxy Disks from the ALMA aRchive (CEDAR). The ALMA archival imaging of nearby ETGs was taken for a variety of purposes and with a variety of spectral setups, sensitivities, and angular resolutions, which complicates the analysis. From this heterogeneous sample, we analyzed the data as uniformly as possible and provide CO line and continuum data products for future study. This CEDAR sample will help to explore molecular gas properties in the extreme radiation field and deeper gravitational potential at the centers of ETGs. Because many host very dynamically cold CNDs, these CO tracers are the most sensitive possible kinematic probes of the inner $\sim$kpc of these massive galaxies. In addition to CO morphological and kinematic information, these ALMA data will, in some cases, reveal thermal emission from cold dust grains and allow for holistic studies of dust longevity, disk formation, and SF processes. The sample also has the potential to add to the collection of existing BH mass measurements that will help tighten existing BH mass-host galaxy scaling correlations. The deeper ALMA CO imaging in CEDAR extends the work of previous local ETG surveys by expanding to CNDs with $M_{H_2} \lesssim 10^7$ $M_\odot$.

The work in this thesis builds upon work begun by Dr. Ben Boizelle as a graduate student at UC Irvine, and continued by undergraduates at BYU such as Joshua Jones, Edison Carlisle, Ben Derieg, and Connor Camacho (Camacho 2024; Carlisle 2023; Derieg 2024; Jones 2023).

This thesis is organized as follows. In Chapter 2, I introduce the ETGs in our sample and describe the archival ALMA observations. In Chapters 3 and 4, I discuss trends across the sample and explore prospects for probing star formation, constraining thermal dust properties, and analyzing gas kinematics. I discuss next steps and conclusions in Chapter 5. Throughout this work, I adopt a standard ΛCDM cosmology with $\Omega_m = 0.308$, $\Omega_{vac} = 0.692$, and Hubble constant $H_0 = 73$ km s^{-1} Mpc^{-1} (Blakeslee et al. 2021; Kenworthy et al. 2022; Riess et al. 2022).

Chapter 2

Data & Methods

In this chapter, I describe the criteria used to select the CEDAR sample and the procedures employed to process archival ALMA observations into science-ready data products.This archival sample encompasses some $\sim$40 distinct ALMA projects and includes nearly 150 low-J ^{12}CO data cubes spanning 118 different ETGs. Nearly three-quarters of these galaxies show clear CO emission, making the sample broadly representative—though not strictly unbiased—of the molecular-gas properties local dust-disk ETGs.

2.1 Sample Selection

From the ALMA archive, we obtained 12-m imaging of ETGs in the low-J ^{12}CO transitions ($J = 1-0$, $2-1$, and $3-2$; hereafter CO). Targets were selected from Cycles $2-5$ to avoid the inherent difficulties in reconstructing and utilizing Early Science data products. For the Cycle 5 data, we focused on more disk-like cases to ensure a manageable sample and to limit the data volume. Many of these CO data have been published previously in some form. Galaxy classification primarily relied on the RC3 catalogue (de Vaucouleurs et al. 1991), although we included a few targets that are classified as ETGs in other literature sources. To avoid contaminating the survey

with galaxies having dubious morphological classifications, we restricted target selection to $z \lesssim 0.05$ or a limiting luminosity distance $D_L \sim 250$ Mpc. In order to at least partially resolve gas properties for local ETGs, we rejected those with average synthesized beam FWHM of be $\theta_{\rm FHWM} \gtrsim 1''$. This criterion corresponds to physical scales of $\gtrsim$100 pc at $D_L \sim 20$ Mpc or $\gtrsim$500 pc at $D_L \sim 100$ Mpc. For projects or observations that push the limits of our selection criteria, we have used our best judgment on a case-by-case basis to balance between sample volume and consistency.

Several targets have extensive observation histories across many cycles and/or array configurations, and may have imaged multiple CO line transitions as well as other molecules or isotopologues. In such cases, we generally analyzed all ALMA CO ETG imaging but focus here on those with sufficient angular resolution to map out the CND kinematics. Data sets with very high angular resolution were generally avoided as well as those with insufficient line sensitivity or too narrow a maximum recoverable scale (MRS) to probe the bulk of the CND properties. We also rejected a handful of targets that are known to be mergers (e.g., NGC 695, NGC 1266), that have significant radial flows or feedback (e.g., Centaurus A, IC 5063, NGC 1316), or that have bright AGN and only absorption-line features (e.g., M87).

The CEDAR sample extends below the ATLAS^{3D} magnitude cutoff for completion and out to greater distances than the MASSIVE survey. The CEDAR sample is heterogeneous, following the distinct observing set-ups for 41 separate ALMA 12-m projects. As a consequence, the CEDAR sample is not unbiased, with a significantly higher percentage of elliptical and cD galaxies relative to those classified as S0, SA0, SB0, etc., than in volume-limited surveys ($\sim$25% ellipticals; Cappellari et al. 2011). Also, the CEDAR targets appear to be biased towards higher central $\sigma_\star$ and presumably higher $M_{\rm BH}$. That being said, CEDAR spans a very broad range of the galaxy parameter space with ALMA CO imaging that is much superior in sensitivity and resolution compared to most previous interferometric CO imaging (e.g., with the Combined Array for Research in Millimeter-wave Astronomy, or CARMA, with $\overline{\theta}_{\rm FWHM} \sim 4''$ for a subsample of ATLAS^{3D}; Alatalo et al. 2013).

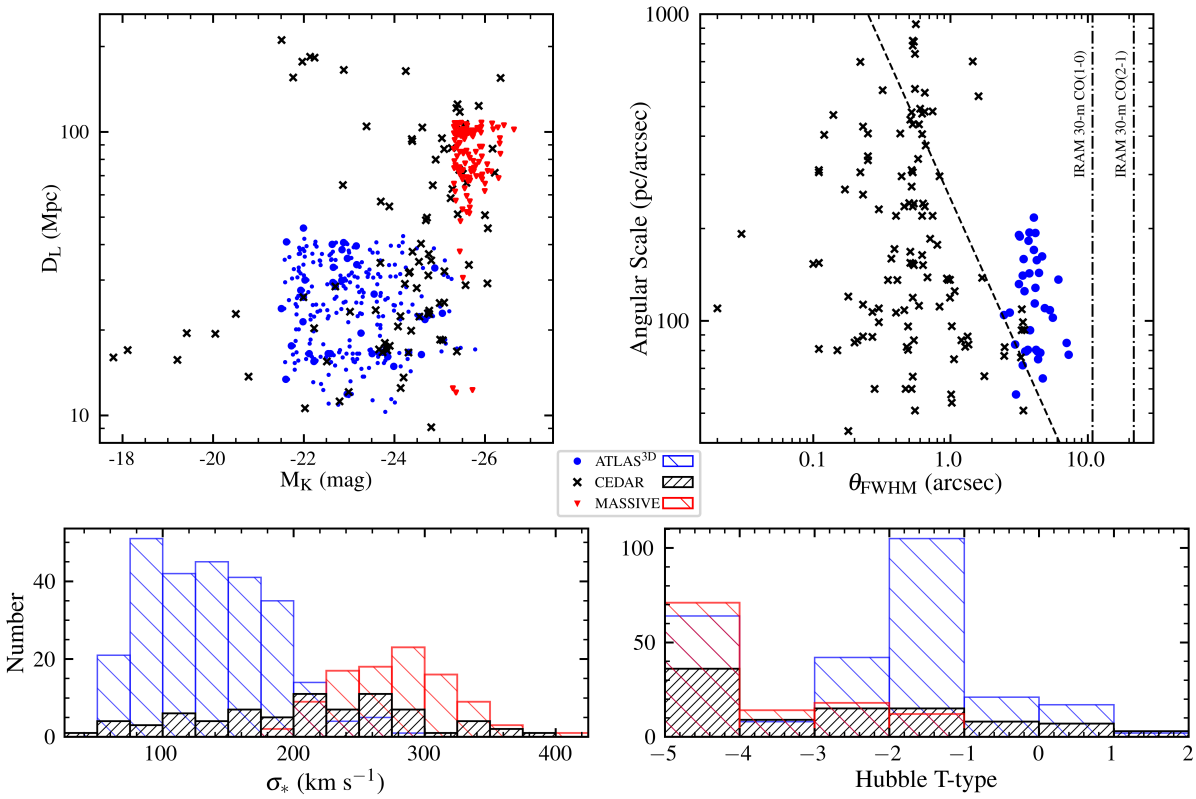

Figure 2.1 Galaxy properties (*top left, bottom panels*) of the CEDAR sample compared to the ATLAS^{3D} and MASSIVE ETG surveys. CO imaging properties from CEDAR and the CARMA subsample of ATLAS^{3D} (*top right*; Alatalo et al. 2013) show clear delineation between ALMA CO capabilities and those of previous interferometric or single-dish surveys (e.g., the IRAM 30-m; Young et al. 2011). The dashed line corresponds to a physical resolution of 250 pc. Supplementary data for the ATLAS^{3D} sample were obtained from Hyperleda.

Because of the northern focus of ATLAS^{3D} ($\delta \gtrsim -6°$) and the southern vantage of ALMA, CEDAR and ATLAS^{3D} have only a few targets in common. The MASSIVE survey has sparse ALMA 12-m imaging, several of which are included in this Cycles 2–5 census.

When possible, we adopted galaxy luminosity distances (D_L) from surface brightness fluctuation (SBF) distance modulus $m - M$ measurements for most of our ETGs (citations; e.g., Gangan-deep+24). For two galaxies, we use Type Ia supernovae (SNe Ia) distance moduli (citations). For the remaining galaxies we followed (Davidson et al. 2024) in estimating D_L from Hubble flow

velocities using the Virgo + Great Attractor + Shapley inflow model (Mould et al. 2000; Wright 2006). We assumed the corrected redshifts from the NASA/IPAC Extragalactic Database (NED[1]) are entirely cosmological in nature, with redshift errors giving $\sim$7% formal uncertainties in the Hubble flow-derived $m-M$.

2.2 ALMA Data Processing

Most of the programs in this archival sample focused on CO emission-line properties, with the redshifted CO transition being centered in one of the spectral windows (spw) while the remaining 2–3 spw measured the continuum in adjacent basebands. Occasionally, additional line tracers [e.g., CS(5−4) in Band 6] lie in one of these other basebands, but usually at much lower S/N. Typically, each spw has a $\sim$2 GHz bandwidth, which spans an observed-frame velocity range of about 5200 km s^{-1} (2600 km s^{-1}) in Band 3 (Band 6). The low-J CO emission only covers a portion of these spw, allowing for good continuum subtraction. For CO(3−2) though, the observed line-of-sight (LOS) velocity extrema ranges up to $\Delta v_{\rm max} \sim 1200$ km s^{-1} comes closer to the full spw extent. In most cases, the CO-line spw was imaged using the frequency division mode (FDM) while many of the other spw were imaged in time division mode (TDM).

For each target, we performed calibration and imaging processes using the appropriate version of the `Common Astronomy Software Applications` (`CASA`; McMullin et al. 2007). Initial pipeline calibration was performed using the delivered `scriptForPI.py` file. This included WVR correlations initial phase and bandpass correction using nearby quasars from the ALMA Calibrator Source Catalogue (CSC). Flux calibration steps use Solar System standards such as Titan, Ceres, Ganymede, and others when available, or brighter quasars from the CSC. These flux standards give absolute flux confidence of $\sim$5% and 10% in Band 3 and Bands 6+7, respectively (Fomalont et al. 2014)

[1] https://ned.ipac.caltech.edu/

Galaxy	T Type	v_{sys} (km s^{-1})	z	$m-M$ (mag)	D_L (Mpc)	D_A (Mpc)	Angular Scale (pc arcsec^{-1})	σ_* (km s^{-1})	M_{K_s} (mag)
(1)	(2)	(3)	(4)	(5)	(6)	(7)	(8)	(9)	(10)
2MASXJ09033081-0106127	-2.0	12156	0.040548	36.17	171.6	158.5	0.769	–	–
2MASXJ13333299+2616190	2.2	11616	0.038747	36.07	163.8	151.8	0.736	–	-24.25
CGCG 013-092	0.4	11037	0.036816	35.96	155.4	144.6	0.701	–	-21.77
CIG 0501	0.0	7488	0.024977	35.10	104.5	99.5	0.482	–	-23.39
CIG 0956	-0.1	8922	0.029761	35.48	125.0	117.9	0.571	–	-25.39
CIG 1044	-2.0	6765	0.022566	34.87	94.3	90.2	0.437	119.2	-24.38
ESO 208-G021	-3.1	942	0.003142	30.66	13.6	13.5	0.066	147.6	-22.74
ESO 322-G08	-2.0	2404	0.008019	32.86	37.3	36.7	0.178	201.6	-24.03
ESO 359-G002	-3.4	1354	0.004516	31.44	19.4	19.2	0.093	53.4	-20.05
ESO 428-G014	-1.8	1693	0.005647	31.82	23.2	22.9	0.111	113.1	-23.02
ESO 443-G024	-3.0	6274	0.020928	34.71	87.3	83.8	0.406	277.3	-26.17
FCC 032	-5.0	1240	0.004136	31.15	17.0	16.9	0.082	–	-18.11
FCC 207	-4.5	1345	0.004486	31.02	16.0	15.9	0.077	60.0	-17.80
FCC 282	-5.0	1145	0.003819	30.98	15.7	15.6	0.076	47.7	-19.21
GAMA 064646	1.3	11723	0.039104	36.09	165.4	153.1	0.742	–	-22.88
GAMA 177186	-5.0	14823	0.049444	36.62	210.6	191.3	0.927	–	-21.51
GAMA 272990	-2.0	12906	0.043050	36.31	182.6	167.8	0.814	–	-22.24
GAMA 622305	0.0	12991	0.043333	36.32	183.8	168.8	0.819	–	-22.14
GAMA 622429	-0.2	12510	0.041729	36.24	176.8	162.9	0.790	–	-21.97
IC 1024	-1.8	1893	0.006314	32.08	26.1	25.7	0.125	75.3	-21.99
IC 1459	-4.8	1864	0.006218	32.33	29.2	28.8	0.140	296.1	-26.05
IC 1531	-2.7	7638	0.025478	35.14	106.7	101.4	0.492	224.9	-25.56
IC 4296	-4.9	3042	0.010147	33.53	50.8	49.8	0.241	327.4	-26.00
IC 4374	-2.8	7348	0.024510	35.05	102.5	97.7	0.474	259.2	-25.47
IC 5063	-1.2	3605	0.012025	33.49	49.8	48.7	0.236	152.3	-24.72
MCG-06-08-024	-4.5	1749	0.005834	31.45	19.5	19.3	0.093	–	-19.42
NGC 0315	-4.1	4844	0.016158	34.30	72.3	70.0	0.339	293.6	-26.32
NGC 0383	-2.9	4996	0.016665	34.10	66.1	64.0	0.310	272.9	-25.59
NGC 0384	-4.2	4105	0.013693	33.77	56.8	55.3	0.268	244.1	-23.70
NGC 0449	0.9	4685	0.015628	34.06	64.9	63.0	0.305	83.2	-22.86
NGC 0507	-3.3	4831	0.016115	33.95	34.0	32.9	0.159	292.1	-25.64
NGC 0524	-1.2	2344	0.007819	31.74	22.3	22.0	0.106	236.7	-24.55
NGC 0547									
NGC 0612	-1.2	8823	0.029430	35.46	123.6	116.6	0.565	–	-25.86

Galaxy	T Type	v_{sys} (km s^{-1})	z	$m-M$ (mag)	D_L (Mpc)	D_A (Mpc)	Angular Scale (pc arcsec^{-1})	σ_* (km s^{-1})	M_{K_s} (mag)
(1)	(2)	(3)	(4)	(5)	(6)	(7)	(8)	(9)	(10)
NGC 0665	-2.0	5291	0.017649	34.33	73.5	70.9	0.344	180.3	-25.43
NGC 0708	-4.9	4664	0.015557	33.83	58.3	56.5	0.274	221.8	-25.24
NGC 0997	-3.9	6300	0.021015	34.71	87.7	84.1	0.408	–	-25.26
NGC 1052	-4.7	1433	0.004780	31.28	18.0	17.8	0.086	208.0	-23.79
NGC 1194	-0.7	3947	0.013166	33.69	54.6	53.2	0.258	–	-23.89
NGC 1326	-0.7	1283	0.004280	31.23	17.6	17.5	0.085	111.2	-23.90
NGC 1332	-2.9	1553	0.005180	31.80	22.9	22.7	0.110	294.6	-24.74
NGC 1370	-3.7	1000	0.003336	30.68	13.7	13.6	0.066	68.9	-20.78
NGC 1380	-2.3	1814	0.006051	31.99	25.0	24.7	0.120	214.5	-25.10
NGC 1386	-0.7	774	0.002582	30.13	10.6	10.6	0.051	133.1	-22.03
NGC 1387	-2.8	1223	0.004079	31.57	20.6	20.4	0.099	167.3	-24.08
NGC 1399	-4.6	1349	0.004500	31.34	18.5	18.3	0.089	332.2	-25.01
NGC 1407	-4.5	1714	0.005717	32.30	28.8	28.5	0.138	265.6	-25.57
NGC 1439									
NGC 1453	-4.7	3771	0.012579	33.55	51.2	49.9	0.242	318.0	-25.40
NGC 1574	-2.9	914	0.003049	31.49	19.9	19.8	0.096	203.7	-24.37
NGC 1600	-4.6	4582	0.015284	34.28	71.7	69.6	0.337	331.4	-26.22
NGC 1684	-3.9	4373	0.014587	33.99	62.8	61.0	0.296	273.8	-25.28
NGC 2110	-3.0	2308	0.007699	32.51	31.8	31.3	0.152	261.6	-24.32
NGC 2865	-4.2	2768	0.009233	32.89	37.8	37.1	0.180	170.8	-24.40
NGC 2872	-4.8	3530	0.011775	33.44	48.8	47.7	0.231	272.5	-24.69
NGC 3078	-4.8	2670	0.008906	32.73	35.2	34.6	0.168	243.3	-24.81
NGC 3081	0.0	2499	0.008336	32.69	34.5	33.9	0.164	118.8	-23.69
NGC 3100	-2.0	2690	0.008973	32.85	37.1	36.4	0.177	190.9	-24.76
NGC 3245									
NGC 3258	-4.3	2872	0.009580	32.53	32.1	31.5	0.153	261.0	-24.34
NGC 3268	-4.3	2782	0.009280	32.71	34.8	34.2	0.166	228.6	-24.54
NGC 3271									
NGC 3377	-4.8	507	0.001691	30.25	11.2	11.2	0.054	136.1	-22.79
NGC 3489	-1.2	492	0.001641	30.41	12.1	12.1	0.058	104.2	-22.99
NGC 3557	-4.9	2958	0.009867	33.30	45.7	44.8	0.217	270.3	-26.06
NGC 3585									
NGC 3599	-2.0	704	0.002348	31.54	20.3	20.2	0.098	65.7	-22.23
NGC 3607	-3.2	909	0.003032	31.79	22.8	22.7	0.110	222.2	-24.77
NGC 3862	-4.8	7016	0.023403	34.95	97.8	93.4	0.453	265.1	-25.41
NGC 4061	-5.0	7885	0.026302	34.94	95.0	90.2	0.437	477.2	-25.05
NGC 4261									
NGC 4374	-4.4	1019	0.003399	31.32	18.4	18.3	0.089	277.6	-25.07
NGC 4429	-0.8	1014	0.003382	31.11	16.7	16.5	0.080	173.4	-24.31
NGC 4435	-2.1	1019	0.003399	31.11	16.7	16.6	0.080	155.0	-23.74
NGC 4438	0.6	-27	-0.000090	31.12	17.0	17.0	0.082	135.3	-23.84
NGC 4477	-1.7	1020	0.003402	31.20	17.4	17.3	0.084	172.5	-23.82
NGC 4594	1.1	1070	0.003569	29.79	9.1	9.0	0.044	225.7	-24.81
NGC 4596	-0.8	1009	0.003366	31.17	17.1	17.0	0.082	140.6	-23.66

Galaxy	T Type	v_{sys} (km s^{-1})	z	$m-M$ (mag)	D_L (Mpc)	D_A (Mpc)	Angular Scale (pc arcsec^{-1})	σ_* (km s^{-1})	M_{K_s} (mag)
(1)	(2)	(3)	(4)	(5)	(6)	(7)	(8)	(9)	(10)
NGC 4636	-4.8	443	0.001478	30.67	13.6	13.6	0.066	199.5	-24.2
NGC 4649	-4.6	1013	0.003379	31.08	16.5	16.4	0.079	330.5	-25.3
NGC 4696	-3.8	4347	0.014500	32.75	35.50	34.5	0.167	242.9	-25.6
NGC 4697	-4.5	1533	0.005114	30.49	12.5	12.4	0.060	165.2	-24.14
NGC 4742	-4.6	1455	0.004853	30.95	15.5	15.4	0.074	101.3	-22.51
NGC 4751	-2.8	1707	0.005694	31.86	23.5	23.2	0.113	350.6	-23.59
NGC 4786	-4.3	5131	0.017115	34.26	71.2	68.8	0.334	284.7	-25.51
NGC 4797	-2.6	8410	0.028053	35.35	117.7	111.3	0.540	201.7	-25.44
NGC 5044	-4.8	2864	0.009553	32.47	31.2	30.6	0.148	224.7	-24.75
NGC 5084	-2.0	1698	0.005664	31.85	23.4	23.1	0.112	199.8	-24.77
NGC 5193									
NGC 5208	-1.9	7463	0.024894	35.09	104.2	99.2	0.481	–	-25.55
NGC 5813	-4.9	2380	0.007939	32.54	32.2	31.7	0.154	236.0	-25.10
NGC 5838	-2.6	1625	0.005420	31.75	22.4	22.1	0.107	273.6	-24.13
NGC 5846	-4.8	2122	0.007078	31.98	24.9	24.6	0.119	237.2	-25.00
NGC 5898	-4.3	2196	0.007325	32.32	29.1	28.7	0.139	204.8	-24.23
NGC 6861	-2.7	3039	0.010137	32.24	28.1	27.5	0.134	387.2	-24.49
NGC 6958	-3.7	2923	0.009750	33.03	40.3	39.6	0.192	185.2	-24.59
NGC 7075	-3.8	5742	0.019153	34.51	79.8	76.8	0.373	256.6	-24.91
NGC 7465	-1.8	2071	0.006908	32.27	28.5	28.1	0.136	94.9	-22.69
NGC 7592	-1.0	7267	0.024240	35.03	101.4	96.6	0.469	–	–
PGC 11179	-2.3	6653	0.022192	34.84	92.7	88.7	0.430	290.8	-24.40
PGC 13571	0.3	1657	0.005527	31.79	22.8	22.5	0.109	–	-20.50
PGC 43387	-4.8	7426	0.024771	35.08	103.6	98.7	0.479	213.5	-24.62
PKS 0718-34	-3.1	8658	0.028880	35.42	121.2	114.5	0.555	–	-25.37
PKS 1718-649	1.8	4674	0.015591	34.06	64.8	62.8	0.305	–	-24.85
UGC 02698	-4.8	6245	0.020831	34.70	86.9	83.4	0.404	362.5	-25.10
UGC 09799	-4.8	11003	0.036702	35.95	154.9	144.1	0.699	218.5	-26.34

Table 2.1 CEDAR host galaxy properties. Col. (2) gives the galaxy's morphology type. Cols. (3) and (4) give the systemic velocity and corresponding redshifts from the NASA/IPAC Extragalactic Database (NED) after correcting for the Virgo + Great Attractor + Shapley inflow model (Mould et al. 2000). Col. 5 lists the adopted distance modulus for each target. Cols. (6) and (7) give the D_L and angular size distance (D_A) corresponding to the adopted redshift values and cosmology, with many calculated using the (Wright 2006) cosmological calculator. Col. (8) gives the angular scale from the D_A values. Col. (9) gives the central stellar velocity dispersion taken from the HyperLEDA database (Makarov et al. 2014) Apparent total K-band magnitudes were also taken from HyperLEDA and used in conjunction with the adopted D_L values to estimate M_K values for each galaxy, as reported in Col. (10).

that typically dominate over statistical uncertainties. In later flux or flux density measurements, we include both terms added in quadrature. Some pipeline calibration scripts included manual masking of select visibilities, especially of spw edge channels.

We further processed pipeline-calibrated Measurement Sets (MSs) in `CASA` v.6 to apply phase self-calibration for brighter continuum sources with typical peak flux densities $S_{\rm cont} \gtrsim 50$ mJy beam^{-1} but extending down to $\sim$15 mJy beam^{-1} in some cases. We did not accept phase-only self-calibration results if artifacts increased or if reasonable solution intervals or data averaging did not improve the peak-to-rms dynamic range. For each target, we constructed MFS images using line-free channels (usually $\pm$500 km s^{-1} from the systemic velocity $v_{\rm sys} \equiv cz$) with `CASA tclean`. This included both natural weighting for greater sensitivity to faint, extended emission and Briggs weighting (Briggs 1995) with robust parameter $r = 0.5$ for a good balance between resolution and sensitivity. In the overwhelmingly majority of this sample, we confidently detected at least a central continuum source above $\sim$4$\times$ the limiting sensitivity.

Finally, the continuum was removed in the *uv* plane using line-free channels prior to imaging into CO data cubes using `tclean`. For targets with sufficient line S/N, we settled on CO cubes with 20 km s^{-1} channels and Briggs weighting ($r = 0.5$), although a few high S/N cases allowed for 10 km s^{-1} binning. Those with low-S/N CO or relatively short total integration required either 30$-$40 km s^{-1} channels and either Briggs or natural weighting. Cube properties and the final $\theta_{\rm FWHM}$ are reported in Table 2.2. For a select few targets, ALMA 12-m programs have imaged adjacent CO transitions with the requisite sensitivity and $\theta_{\rm FWHM}$ relative to the disk CO extent $R_{\rm CO}$ to allow for resolved measurements of line ratios. As we discuss in Section 4.4, CO line ratio gradients may reveal changing density or excitation conditions with radius. To make a more reasonable comparison between CO imaging taken in different array configurations, we re-imaged the higher-resolution data set to construct a CO cube with matching restoring beam and velocity binning

2.3 Continuum Products

In addition to CO detection, these ALMA data sets enable sensitive studies of both unresolved and extended continuum emission arising from both thermal and non-thermal processes. The centrally-peaked continuum features likely originates from low-luminosity AGN (LLAGN) as most ETGs show at least some level of nuclear activity (Ho et al. 1997; Nyland et al. 2016). This apparent unresolved central emission is likely some combination of synchrotron and thermal dust emission near the AGN. The vast majority of targets have $S_{\rm cont}$ of a few mJy beam^{-1} at either 115 GHz or 230 GHz.

2.4 Emission-line Products

To characterize CO emission properties, we created moment maps by adapting standard code (Teague & Foreman-Mackey 2018) to allow for manual interactive masking of emission on a channel-by-channel basis. Additional low-level sigma-clipping (typically 2.5$\times$ the rms level) removed negative noise and low confidence emission features. These moment maps were further binned using Voronoi tesselations (Cappellari & Copin 2003) to improve the integrated S/N, especially near the CND edge. In Figures 2.2, 2.3, and 2.4, we show moments 0 and 1 and PVDs for CO-bright cases with a clear disk-like CO distribution.

Next, we constructed velocity profiles for the CEDAR sample, integrating the CO cube flux densities in each channel over an elliptical region. These extraction regions roughly follow the major, minor axes ($R_{\rm maj}$, $R_{\rm min}$) estimates made from the moment 0 maps. Finally, we extracted major-axis position-velocity diagrams (PVDs) from each cube using the Cube Analysis and Rendering Tool for Astronomy (CARTA, Comrie et al. 2021). The major-axis orientation was estimated by eye to match the moment 1 line of nodes across as much of the disk as possible, although some CNDs show more

significant warping signatures that make a single orientation insufficient. Typical spatial-extraction widths are ~ 5 pixels in order to fully cover the synthesized beam FHWM.

We measured CO flux values by both integrating the CO line profiles as well as summing the more confident CO emission that forms the moment 0 maps. For most of our sample, these two line flux values ($S_{\rm CO}\Delta v$; see Table 2.2) agree within their respective (statistical and systematic) uncertainties. However, for a few the CO line profile measurements can be either elevated or suppressed relative to moment 0 total. In the former instance, this could arise if there is significant CO emission that lies below the masking threshold, which is supported by the more limited extent of the CO-bright compared to the dust. In the latter case, interferometry may introduce negative features near CO features.

For a majority of targets in our sample we detect emission in channels spanning $\pm$200$\sim$400 km s^{-1}. The CO emission reveals complicated substructures, including central clumps or holes about the SMBH, resolved giant molecular clouds (GMCs), concentric rings or spiral-like features, and flocculant disks. For a select few of our targets, the highest velocity line emission is found adjacent to the galactic nucleus. This occurs when the observations are able to resolve emission within the SMBH SOI.

Galaxy Name	ALMA Code	CO Transition	$S_{CO}\Delta v$ (Jy km s^{-1})	Channel RMS (Jy beam^{-1})	Disk (maj × min) (arcsec)	Morphology	$R_{\rm hole}$ (arcsec)
(1)	(2)	(3)	(4)	(5)	(6)	(7)	(8)
NGC 4596	2015.1.00989.S	1-0	9.624	1.50E-03	4.3 × 3.1	D	–
NGC 4697	2015.1.00591.S	1-0	3.848	5.30E-04	3.6 × 1.1	D	–
NGC 4697	2015.1.00878.S	2-1	9.131	4.80E-04	3.6 × 0.9	D	–
NGC 4697	2015.1.00598.S	2-1	14.198	7.20E-04	3.8 × 1.2	D	–
NGC 4786	2015.1.00878.S	2-1	7.869	4.50E-04	0.6 × 0.4	D	–
NGC 4797	2015.1.00320.S	1-0	4.385	5.50E-04	3.4 × 1.7	D?	–
NGC 5084	2015.1.00598.S	2-1	2.714	9.00E-04	1.7 × 0.7	D?	1.6
NGC 5208	2015.1.00187.S	2-1	37.583	1.40E-03	15.2 × 3.3	D	6.1
NGC 5838	2015.1.00878.S	2-1	31.916	5.50E-04	1.9 × 0.9	D	–
NGC 5846	2015.1.00860.S	2-1	0.527	4.20E-04	– –	F	–
NGC 6958	2015.1.00466.S	2-1	186.078	5.20E-04	1.4 × 1	D-F	–
NGC 7075	2015.1.01572.S	2-1	0.487	7.50E-04	0.7 × 0.5	D?	–
NGC 7465	2015.1.00989.S	1-0	50.903	9.00E-04	13.1 × 9	D-F	–
PGC 13571	2015.1.00497.S	1-0	5.623	2.00E-03	– –	F?	–
PGC 43387	2015.1.00598.S	2-1	20.919	9.00E-04	3 × 2	D	–
PKS 1718-649	2015.1.01359.S	2-1	77.345	2.80E-04	11.7 × 2.9	D-F	–

Table 2.2 CO Emission properties for targets in the CEDAR sample. Col. (4) gives the integrated CO flux. Col. (5) gives an averaged channel RMS noise value. Cols. (6) gives the size of disk in arcsec. Cols. (7) gives the emission morphology as described in Section 3.2, and Col. (8) give the radius the central hole when detected. (Table continued below)

Galaxy Name	ALMA Code	CO Transition	$S_{CO}\Delta v$ (Jy km s^{-1})	Channel RMS (Jy beam^{-1})	Disk (maj × min) (arcsec)	Morphology	$R_{\rm hole}$ (arcsec)
(1)	(2)	(3)	(4)	(5)	(6)	(7)	(8)
2MASXJ0903	2015.1.00320.S	1-0	9	1.10E-03	6.2 × 1.5	D	–
2MASXJ1333	2015.1.00320.S	1-0	7.495	1.20E-03	5.8 × 1.9	D	–
CGCG013-092	2015.1.00320.S	1-0	13.151	7.90E-04	9.8 × 2.6	D?	–
ESO 428-G014	2015.1.00086.S	2-1	85.276	6.60E-04	9.6 × 6.7	S	–
FCC 207	2015.1.00497.S	1-0	0.44	1.20E-03	– –	D?	–
FCC 282	2015.1.00497.S	1-0	2.035	2.50E-03	– –	?	–
GAMA 064646	2015.1.00477.S	2-1	10.931				
GAMA 272990	2015.1.00477.S	2-1	15.602	6.80E-04	5.1 × 3.7	D	–
GAMA 622429	2015.1.00477.S	2-1	49.702	8.50E-04	1.2 × 0.7	D-F	–
IC 1024	2015.1.00989.S	1-0	66.344	1.40E-03	11.3 × 3.5	D-I	–
IC 1531	2015.1.01572.S	2-1	1.143	7.50E-04	0.7 × 0.6	D?	–
IC 4374	2015.1.00644.S	2-1	2.738	2.80E-04	– –	F	–
NGC 0383	2015.1.00419.S	2-1	73.687	1.80E-03	3.7 × 2.9	D	–
NGC 0449	2015.1.00419.S	2-1	52.632	2.70E-03	7.9 × 2.4	D-F	–
NGC 0524	2015.1.00466.S	2-1	36.633	2.70E-04	6.9 × 6.4	D-R	1.4
NGC 0612	2015.1.01572.S	2-1	280.284	1.30E-03	14.9 × 2.6	D-I	7.3
NGC 0665	2015.1.00187.S	2-1	28.354	4.50E-04	– × –	F	–
NGC 0708	2015.1.00598.S	2-1	16.642	7.50E-03	2.8 × 0.8	D-I	–
NGC 0997	2015.1.00187.S	2-1	106.659	1.10E-03	5.6 × 5	D	1.5
NGC 1326	2015.1.00404.S	3-2	623.889	7.20E-04	7.4 × 5.9	D-F	–
NGC 1332	2015.1.00896.S	2-1	28.667	1.90E-04	2.2 × 0.3	D	–
NGC 1370	2015.1.00989.S	1-0	33.261	1.30E-03	5.4 × 2.6	D-I	–
NGC 1386	2015.1.00497.S	1-0	75.214	2.50E-03	19.3 × 9.8	D-S	–
NGC 1387	2015.1.00497.S	1-0	76.401	2.30E-03	10.9 × 9.8	D	–
NGC 1574	2015.1.00419.S	2-1	15.235	6.10E-04	1.6 × 1.5	D-F	–
NGC 1684	2015.1.00187.S	2-1	103.059	1.90E-03	7.2 × 2.6	D	–
NGC 2110	2015.1.00419.S	2-1	50.204	9.10E-04	5.1 × 5	D-I	–
NGC 2872	2015.1.00878.S	2-1	0.802	1.10E-03	0.5 × 0.4	D?	–
NGC 3078	2015.1.00878.S	2-1	2.456	4.40E-04	0.6 × 0.4	D?	–
NGC 3081	2015.1.00086.S	2-1	74.296	1.30E-03	11.6 × 8	S	–
NGC 3100	2015.1.01572.S	2-1	18.388	5.00E-04	3.3 × 4.5	I	–
NGC 3489	2015.1.00989.S	1-0	12.093	1.10E-03	– × –	F	–
NGC 3557	2015.1.00591.S	1-0	1.608	8.50E-04	1.5 × 1.1	D	–
NGC 3557	2015.1.00878.S	2-1	5.231	4.80E-04	1.1 × 0.7	D	–
NGC 3557	2015.1.01572.S	2-1	5.917	6.50E-04	1.2 × 0.9	D	–
NGC 3599	2015.1.00989.S	1-0	2.193	1.00E-03	1.8 × 1.5	D?	–
NGC 3607	2015.1.00598.S	2-1	128.704	1.30E-03	10 × 7.1	S	–
NGC 3862	2015.1.00598.S	2-1	12.645	1.30E-03	1.1 × 0.9	D?	–
NGC 4061	2015.1.00598.S	2-1	19.864	1.60E-03	2 × 1	D	–
NGC 4435	2015.1.00598.S	2-1	95.81	1.20E-03	3.3 × 1.2	D	–
NGC 4438	2015.1.00598.S	2-1	623.881	1.50E-03	18.3 × 4.4	D-F	–
NGC 4477	2015.1.00989.S	1-0	7.647	1.10E-03	2.8 × 2.2	D-I	–

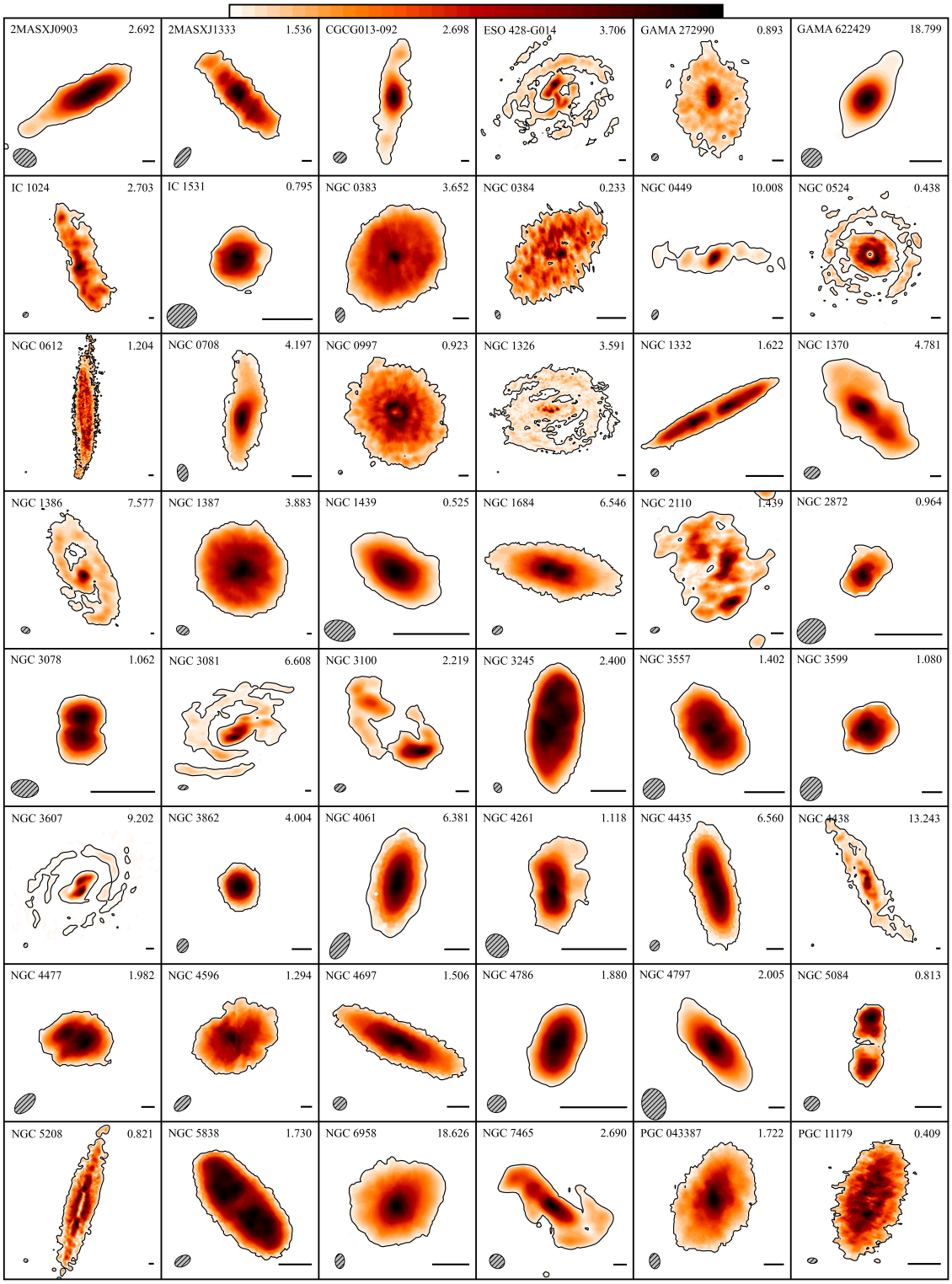

Figure 2.2 CO moment 0 (flux) maps for targets in the CEDAR sample following the color bar (top) with contours plotted as fractions of the maximum flux values printed in the top right (in Jy/beam). For extended and diffuse emission, contours are smoothed using `Scipy` Gaussian filter functions from the `ndimage` package. The synthesized beam area and 2" scale indicator are included (bottom left and right).

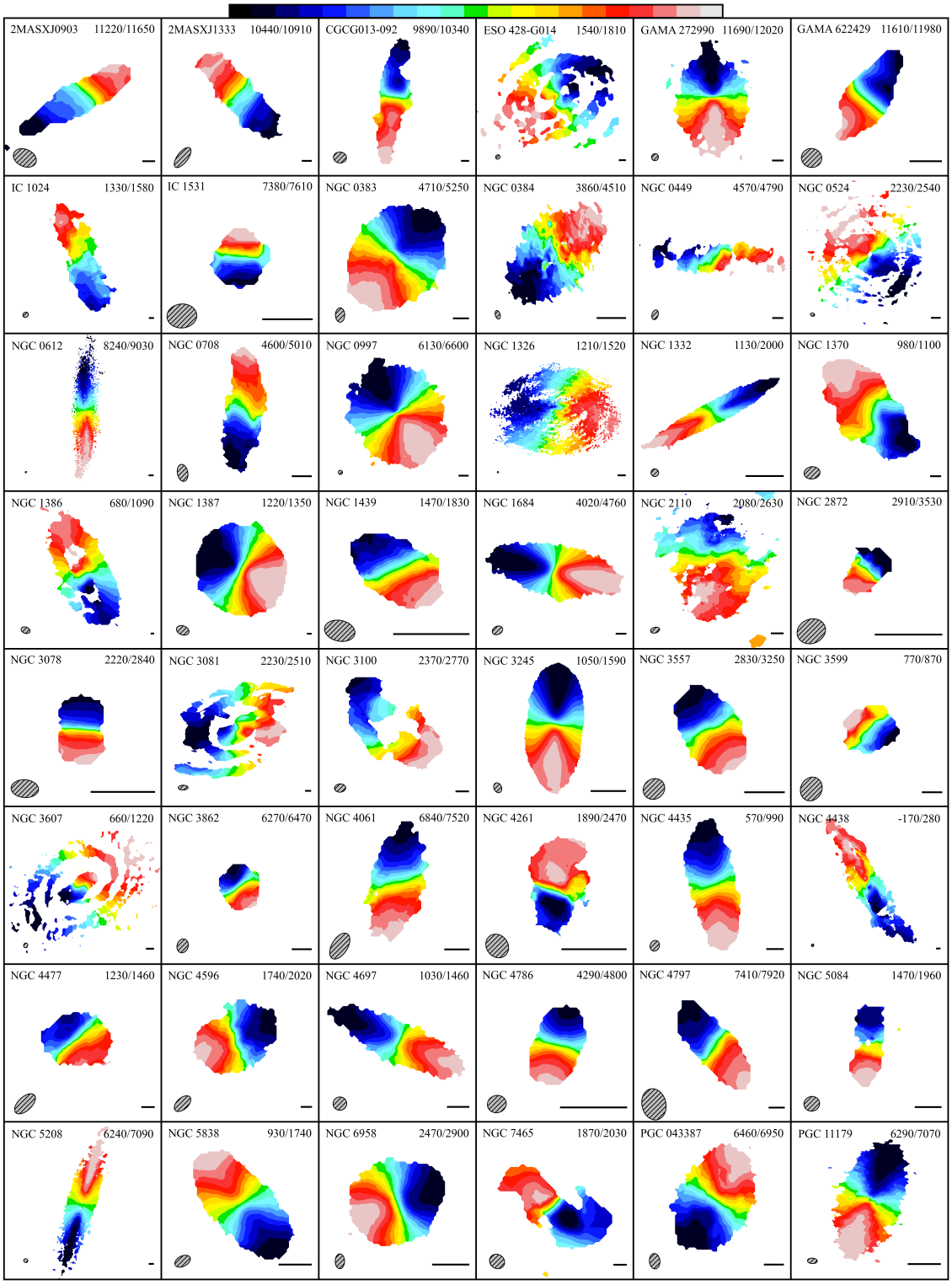

Figure 2.3 CO moment 1 (velocity) maps for targets in the CEDAR sample. Maximum velocity values (km s^{-1}) are given in the top right. Contours of the moment 0 maps are overlaid on the moment 1 maps.

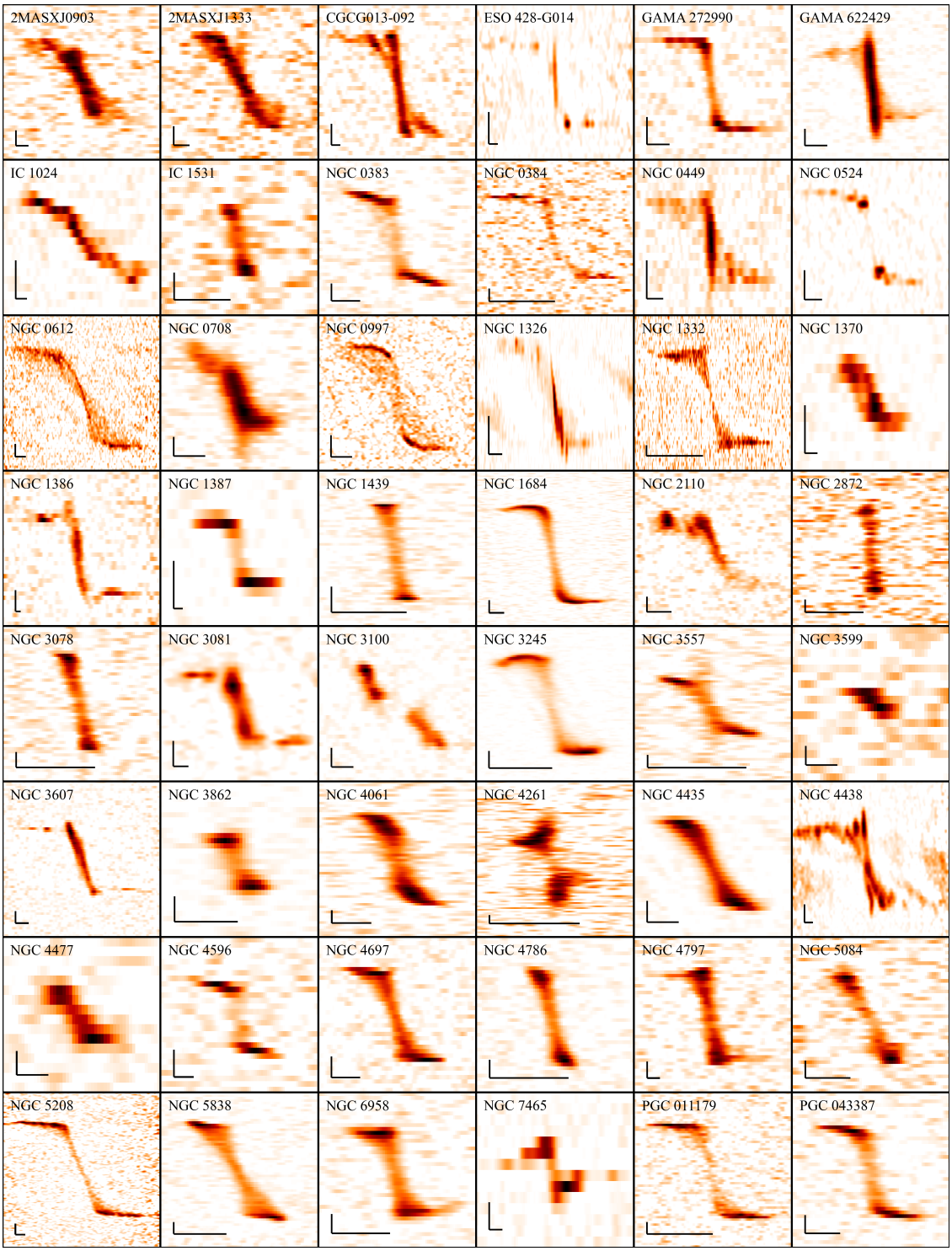

Figure 2.4 Position vs Velocity diagrams (PVDs) for CEDAR galaxies. Scale bars denote 200 km s^{-1}velocity spacing in the y axis and 2" spacing in the x axis.

Chapter 3

Results

We detected line emission in at least 83 of our 118 galaxies with $\gtrsim 3\ \sigma$ confidence. Emission properties for these targets are listed in Table 2.2. The CO emission reveals molecular gas reservoirs with a wide range of morphologies and kinematic behaviors. In this section we describe our methods for calculating molecular gas masses and classifying emission morphology and explore connections between CO/continuum emission properties and host galaxy/SMBH properties.

3.1 Molecular Gas Masses

We estimate the molecular gas masses (M_{H_2}) from observed CO luminosities L'_{CO} using the standard relation $M_{H_2} = L'_{CO}\alpha_{CO}$, where α_{CO} is the CO-to-H_2 conversion factor. CO luminosities are related to observables (Carilli & Walter 2013) by

$$L'_{CO} = 3.25 \times 10^7\, S_{CO}\Delta v \frac{D_L^2}{(1+z)^3 \nu_{obs}^2}\ \text{K km s}^{-1}\ \text{pc}^2 \tag{3.1}$$

where $S_{CO}\Delta v$ is the measured flux of the line in Jy km s^{-1}, D_L is the luminosity distance in Mpc, and ν_{obs} is the observed frequency in GHz. Following standard convention, CO (2-1) and (3-2)

luminosities are are converted to CO (1-0) luminosities using average CO transition ratios

$$R_{21} \equiv \frac{I_{\mathrm{CO(2\text{-}1)}}}{I_{\mathrm{CO(1\text{-}0)}}} = \frac{L'_{\mathrm{CO(2\text{-}1)}}}{L'_{\mathrm{CO(1\text{-}0)}}} \tag{3.2}$$

$$R_{31} \equiv \frac{I_{\mathrm{CO(3\text{-}2)}}}{I_{\mathrm{CO(1\text{-}0)}}} = \frac{L'_{\mathrm{CO(3\text{-}2)}}}{L'_{\mathrm{CO(1\text{-}0)}}} \tag{3.3}$$

where, for example, $I_{CO(2-1)}$ refers to the velocity integrated specific intensity of the CO(2-1) line in temperature units K km s^{-1}. We adopt R_{21} and R_{31} values of 0.65 and 0.5 from (Leroy et al. 2022), which were calculated from single-dish CO mapping surveys and PHANGS-ALMA observations. In addition, we adopt an value for α_{CO} of 3.3 $M_{\odot}$ pc^{-2} (K km s^{-1})$^{-1}$ from a sample of nearby late-type galaxies (Chiang et al. 2024). However, we note that this value is an approximation, as no complete prescription for CO-to-H_2 conversion in ETGs yet exists. Previous studies have shown that α_{CO} can vary with environment, often becoming lower in galactic centers (Teng et al. 2023; see Bolatto et al. 2013; Sandstrom et al. 2013 for a more general discussion on CO-to-H_2 conversion).

The molecular gas masses in our sample span from $10^6 - 10^{10}$ M$_{\odot}$, highlighting substantial diversity in the cold gas content of ETGs (Figure 3.1). This mass range extends beyond previous CO studies (e.g. ATLAS^{3D} Young et al. 2011), revealing smaller molecular gas reservoirs than what was previously observable. In many cases, these value are likely lower limits, as high resolution observations can "resolve out" extended emission. We calculate the molecular gas surface density (Σ_{H_2}) using disk areas determined from the CO flux maps. The resulting surface densities typically range from tens to several hundred $M_{\odot}$ pc^{-2}. Such conditions could be conducive to star formation, given that molecular gas surface density is often strongly correlated with star formation rates (Heiderman et al. 2010; Lada et al. 2012). We observe no obvious dependence of gas surface density or total gas mass on galaxy luminosity, although there is perhaps a tentative trend toward higher Σ_{H_2} in more massive elliptical galaxies.

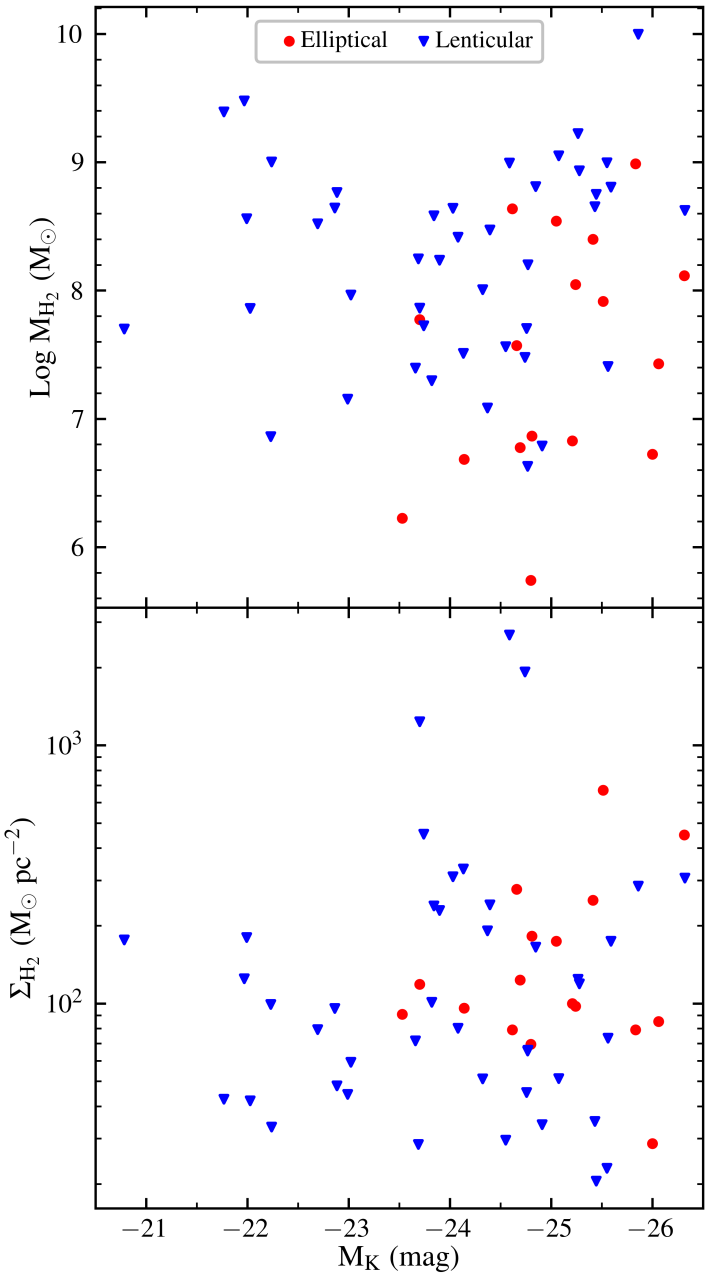

Figure 3.1 CEDAR vs ATLAS^{3D}CO properties. Top panels: histogram of M_{H_2} and Σ_{H_2} surface mass density. Middle panels: M_{H_2} and Σ_{H_2} vs absolute K-band magnitude. Bottom panels: M_{H_2} and Σ_{H_2} vs central velocity dispersion. Dotted vertical line denotes the lower limit M_{H_2} values of the ATLAS^{3D}sample.

3.2 CND Morphologies

CEDAR galaxies display a variety of morphologies and complex substructure in their CO emission. We visually classify the CO emission in our sample according to a scheme similar to Alatalo et al. (2013): regular disks (D), spiral-like (S), rings (R), irregular (I), and diffuse/flocculent (F). These classifications are based primarily on the CO flux maps, with additional guidance from velocity maps and PVDs to identify dynamically disturbed objects. We emphasize that galaxies classified as having a regular disk-like morphology could possess more complex intrisic substructures that only become apparent at high resolution. This is the case for a few targets included in both the CEDAR and CARMA-ATLAS^{3D}samples, such as NGC 3607 and NGC 4435. CARMA barely resolved the central CO emission in these targets revealing only smooth, disk-like morphologies; however, ALMA observations clearly show more complicated substructures (see Figure 3.2). In several high-resolution observations, a central CO deficit or 'hole' is emerges. We note all targets that reveal a central CO hole, and note that the detection of such a hole is heavily dependent on the resolution of the observation.

Most galaxies in our sample feature regular molecular disks, which appear relatively smooth at lower resolutions ($\sim$ 1") but become clumpy at higher resolutions ($\sim$ 0.1"). This behavior likely reflects the fact that these disks intrinsically composed of GMC-scale structures that are only resolved at smaller beam sizes. The prevalence of smooth, regular disks could also have a dynamical explanation, as they reside in steep gravitational potential wells due to massive bulge components which may suppress gravitational instabilities and promote dynamically stable disks. These same processes might also help suppress star formation in these CNDs. Because the molecular gas is dynamically cold, these CNDs are sensitive probes of the central potential and they do not exhibit strong signatures of high turbulence, inflows, or outflows.

CEDAR galaxies that show spiral-like CO substructures include ESO 428-G014, NGC 1386, NGC 3081, and NGC 3607. Notably, they are all lenticular galaxies. It is unclear whether these

features represent genuine spiral arms with distinct kinematics or are simply over-dense regions of a molecular CND. The dearth of spiral-like features in our sample could again stem from the steep potential wells in the central regions of these ETGs, which produce high epicycle frequencies and prevent the gravitational instabilities necessary for the formation of spiral arms. Alternatively, spiral features may be simply unresolved in some targets, blending into an apparently smooth disk structure. Only two CEDAR ETGs (NGC 0524 and NGC 6861) show ring-like disk substructure, as opposed to the 25% detection rate found in the CARMA-ALTAS^{3D} sample.

Disrupted CO morphologies clearly indicate systems that are undergoing or have recently experienced interactions with their environment. External accretion of cold gas or mergers would naturally lead to disrupted molecular gas distributions. Simulations suggest that gas relaxation times can on the order of a few Gyr (van de Voort et al. 2015), implying that the early accretion or merger history of ETGs may be difficult to constrain from CO morphologies alone.

An absence of CO emission in the innermost regions has been demonstrated in many ETG CNDs (Boizelle et al. 2019; 2021), especially at high resolution. These findings suggest that central molecular gas may either be truly absent or poorly traced by low-J CO transitions. Depletion of central molecular gas could be arise from photodissociation in an intense central radiation field, AGN activity (which could ionize or drive out the gas), or disk instabilities from a non-axisymmetric potential. Alternatively, the molecular gas might become so dense in the galactic center that it is better traced by higher critical-density lines (e.g., ^{13}CO, HCN, HCO^{+}, HCN; Jiménez-Donaire et al. 2019; Kauffmann et al. 2017). In contrast, Davis et al. (2018) argued that the opposite may hold: namely the gas density in the very center could fall below the cricial density of low-J CO, if strong BH tidal forces prevent disk fragmentation into clouds (a scenario akin to morphological quenching; see Martig et al. 2013).

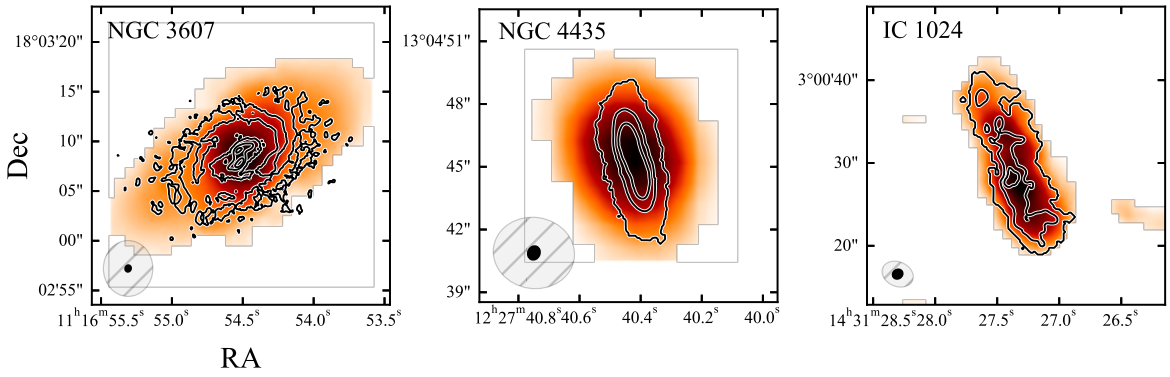

Figure 3.2 Comparison between CARMA CO(1-0) imaging (heat map) and ALMA CO imaging (contours). ALMA observations of NGC 3607 and NGC 4435 are of CO(2-1) while ALMA imaging of IC 1024 is of CO(1-0). In the bottom left corner of the images, primary beams for the CARMA images are given in gray with the ALMA primary beams represented in black. For all of the targets, higher resolution ALMA imaging reveals more complex substructure than that seen with ALMA.

3.3 Kinematic Analysis

To probe the kinematic properties of our sample, we use the KINEMETRY formalism and code (Krajnović et al. 2006), which fits elliptical annuli to two-dimensional kinematic maps and performs a harmonic decomposition along those annuli. In this work, we apply KINEMETRY only to the first moment ($v_{\rm LOS}$) where the dominant k_1 coefficient represents the projected velocity distribution. As the Fourier coefficients are fit, KINEMETRY simultaneously determines the position angle Γ and axial ratio q at each radius. Variations in these parameters indicate disk warping in well-resolved CNDs; however, they may also be affected by observational effects such as beam smearing in poorly resolved cases. As such, we limit our kinematic analysis to observations that span at least $\gtrsim 3$ resolution elements across the disk major axis.

To isolate non circular components, we extract the circular velocity from the KINEMETRY fits and subtract these model velocities from the real velocity field. The largest residuals typically appear in the disk center, where beam smearing is most significant, or at the disk edges, where

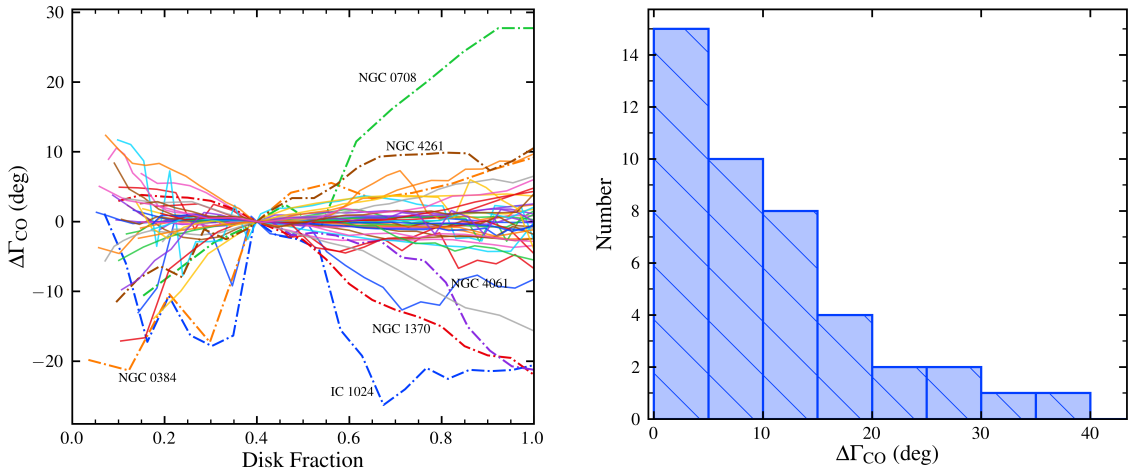

Figure 3.3 Total variation in CO kinematic PA for CEDAR galaxies. Left: Normalized Kinematic PA as a function of disk radius, normalized at R_{disk} = 0.4. Right: Histogram of $\Delta\Gamma$

low signal-to-noise degrades the fit quality. In most cases, these residuals are of the same order as the native cube channel velocity spacing. Hence, the small residuals for many CEDAR galaxies suggest that the molecular gas kinematics are well-described by regular circular rotation. Figure 3.3 illustrates the variation in CND kinematic PA (Γ_{CO}) as a function of radius for CEDAR galaxies. Overall, CEDAR CNDs appear to be highly ordered, with most kinematic PA variations $\lesssim 15°$ across the disk (Figure 3.3).

High resolution CO imaging of a select few ETGs (combined with tilted-ring dynamical modeling) has revealed either disk warping (Boizelle et al. 2019) or complicated non-circular motion (perhaps not necessarily pure radial inflows/outflows; Zhang et al. 2025). The fact that this warping and/or non-circular motion coexists with otherwise relaxed molecular gas kinematics regular dust-disk morphologies may indicate ongoing settling process or perturbations from a triaxial galaxy potential (Emsellem et al. 2011). In galaxies featuring more irregular dust lanes or non-relaxed kinematics (e.g. IC 1024, NGC 0708), any detected noncircular motion could point to recent merger activity or ongoing external accretion.

CND/Host-Galaxy Alignment

Kinematic misalignment between gas and stars can shed illuminate the evolutionary history of the galaxy. Initially, stellar-gas misalignment was attributed primarily to mergers, but analytical models that consider only mergers under predict the observed fraction of misaligned ETGs (Davis & Bureau 2016). Instead, simulations that incorporate multiple pathways – mergers, gas stripping, interactions with the environment, and secular processes such as filament accretion or misaligned halo cooling– reproduce the observed misalignment rates (Baker et al. 2024; Khim et al. 2021). More precise measurements of the stellar-gas misalignment fraction in the local universe, as well as the identification of strongly misaligned systems, are crucial for constraining the role tehse processes play in shaping ETG evolution.

Previous studies have compared stellar and gaseous kinematics using integral-field spectroscopy (e.g. SAURON: Bacon et al. 2001; Davis et al. 2011; SAMI Bryant et al. 2019). However, because comprehensive IFU data are unavailable for many of our targets, we here compare only the molecular gas kinematics to stellar isophotes measured from HST imaging (with many measurements from Davidson et al. 2024). (Krajnović et al. 2011) found that up to 90 percent of local ETGs (ATLAS^{3D}targets) show $\lesssim 5^\circ$ alignment between their global stellar photometric and kinematic PAs. By contrast, (Ene et al. 2018) reported a much higher fraction of misalignment among more massive ETGs (MASSIVE targets), with 30 out of 71 rotators exhibiting misalignment $> 15^\circ$ between global kinematic and photometric PA. Most of these misaligned systems were slow rotators. Hence, it appears that low-z ETGs are typically well aligned in stellar-isophotes and kinematics, except in triaxial or disturbed objects.

A common classification labels gas-stellar angles $\psi = |\mathrm{PA}_{\mathrm{gas}} - \mathrm{PA}_{\mathrm{stars}}| < 30^\circ$ as aligned and misaligned when $\psi > 30^\circ$ (Davis et al. 2011). One caveat that needs mentioning when using photometric PAs is the 180° degeneracy between stable counter-rotation ($\psi > 150^\circ$) and true alignment. Whereas the kinematic PAs is physically defined as the counterclockwise angle between

north and a line bisecting the velocity field (relative to on the receding side), the stellar-isophotal PA is determined by major axis of the best-fit ellipse to the light distribution, which does not distinguish between a rotation of ϕ and $\phi + 180°$. For clarity, in this work we define ψ such that $0° \leq \psi \leq 90°$ and apply the same convention to prior data for consistent comparisons.

Figure 3.4 shows the distribution of gas-stellar alignment values for our sample. Most CEDAR galaxies exhibit a high degree of alignment, with most having $\psi \lesssim 5°$. Because the ALMA data provide sufficiently high resolution, we can also compare global PA values at different radii. In some galaxies, the central stellar distribution is heavily attenuated by dust associated with the molecular disk, so we exclude those radii from the comparison. Only two galaxies show significant misalignment: NGC 1387 and NGC 5193. The nearly face-on inclination of NGC 1387 (axis ratio $\sim$0.98) introduces large uncertainties in the derived PA.

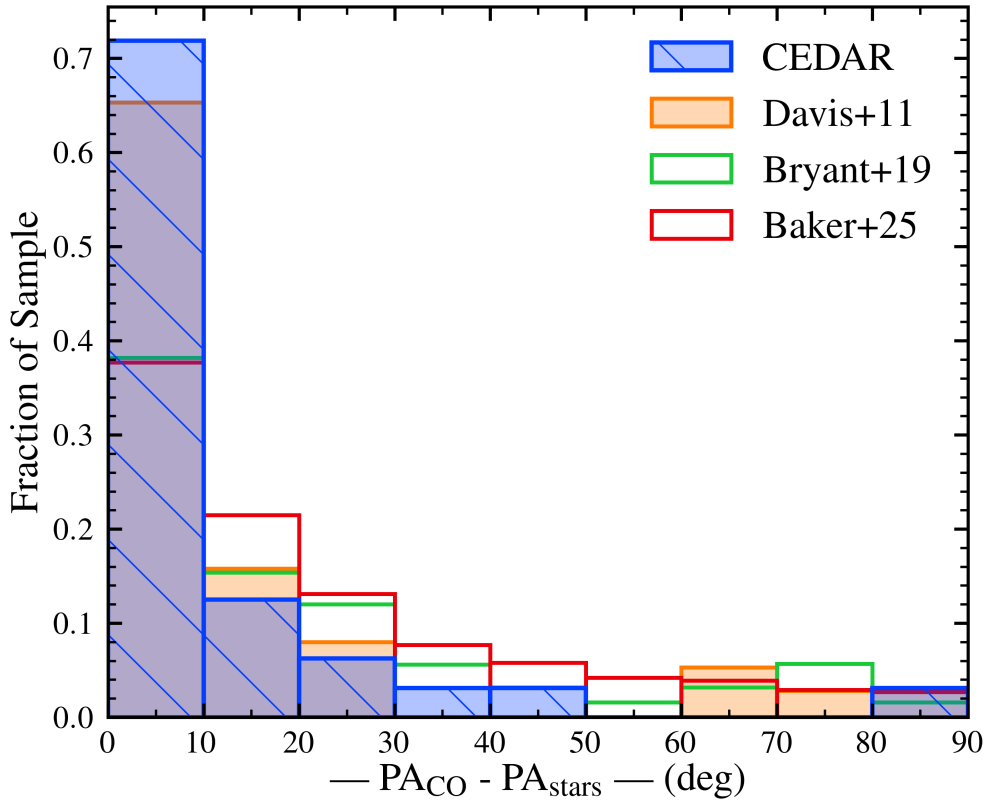

Figure 3.4 Histogram of $\psi = |\mathrm{PA_{gas}} - \mathrm{PA_{stars}}|$ values. The dotted line at 30° denotes the standard threshold between alignment and misalignment. Results compared to (Baker et al. 2024; Bryant et al. 2019; Davis et al. 2011)

Chapter 4

Discussion

We have demonstrated that ETGs across a vast galaxy parameter space host molecular CNDs traced by CO emission. While these CNDs have varying sizes (both absolute and relative to their host galaxy) and demonstrate a variety of complex substructure when well resolved, kinematic modeling of these CNDs suggest ordered, disk-like rotation that is well aligned with the stellar population. The exploitation of these molecular CNDs as stable probes of central galactic gravitational potential has been done extensively since the advent of ALMA, providing some of the most precise SMBH calculations to date. However, vital details for these CND remain unclear. Such details include their formation/evolution through cosmic time, their proclivity/ability to form new stars, and their role in SMBH feeding/feedback processes. Ironing out these details are sure to shed light on galaxy evolution processes, particularly those processes connecting SMBH/host-galaxy growth suggested by BH scaling relations.

4.1 Formation of Molecular CNDs

The molecular CNDs can arise from two channels: *in situ* generation through stellar evolution and feedback or *ex situ* generation via gas accretion and merger events. Stellar evolution models suggest

an average stellar population can return a fraction of their mass to the ISM, roughly on order of half of its mass over the current age of the universe. Expelled gas from gradual mass loss – red giant/asymptotic giant branch stars and planetary nebulae – joins the galaxy's hot gas reservoir over time. Under the right conditions this hot gas could cool, fall towards the galaxy center, and build up a central molecular gas reservoir. This gradual stellar mass loss should basically be a continuous process and one that is determined almost entirely from the number of stars present in the galaxy and its star formation history. We have demonstrated, consistent with previous work (Young et al. 2011; 2014), that there is no strong connection between molecular gas and host-galaxy properties (Figure 3.1). Low CO detection rates that are independent of host luminosity (lower limit of 22%, Young et al. 2011) further suggest that *in situ* generation of molecular does not ubiquitously occur at a rate fast enough to replenish molecular gas reservoirs in ETGs.

This leaves external generation of molecular gas (through either cold gas accretion or merger events) as the likely channel for the formation of molecular CNDs in ETGs. Characterizing the alignment between between gas and stars has been a promising avenue for constraining the lower limit of externally acquired gas, as clear misalignment between gas and stars is strong evidence that the gas was recently acquired and is still settling into the host galaxy.

4.2 Star Formation in ETGs

A critical question regarding our sample of ETG CNDs is whether the molecular gas is actively forming stars. The existence of a bimodality in galaxy type strongly supports a scenario in which physical processes turn a star-forming blue cloud galaxy into a passive red sequence galaxy, with star formation eventually being quenched. Understanding the star formation rates (or lack therof) in ETGs would provide further observational evidence on the nature of the quenching mechanism. Many of the proposed quenching channels, such as ram pressure stripping or AGN feedback, cease

star formation by removing molecular gas and starving star formation. However, such mechanisms would likely not be in play should the molecular gas be regenerated in the galaxy. Other quenching mechanisms, such as morphological quenching (Martig et al. 2009; 2013) would render molecular CNDs stable against collapse and thus unable to form new stars. Initial analysis of CND stability using the Toomre local stability parameter found them to be stable against collapse (Boizelle et al. 2017).

4.3 Supermassive black holes

Despite only gravitationally dominating the innermost region of galaxies, supermassive BHs have been shown to be intimately related to the large-scale evolution of their host galaxy (Kormendy & Ho 2013). Empirical scaling relations reveal that BH masses ($M_{\rm BH}$) strongly correlate with properties such as stellar velocity dispersion (σ_*; Ferrarese & Merritt 2000; Gebhardt et al. 2000) and stellar bulge luminosity (L; Kormendy & Richstone 1995). These relations suggest that BHs and galaxies evolve in lockstep through a process of accretion and merger events. Nonetheless, a complete physical description of the coevolution of supermassive BHs and their host galaxies is still lacking.

A representative BH census, one in which the wide range of host galaxy properties is fully reflected, is necessary to understand this interplay. To date, slightly more than $\sim$100 dynamical measurements of $M_{\rm BH}$ have been performed, mostly by modeling stellar or gas kinematics (Kormendy & Ho 2013; Saglia et al. 2016). We have compiled these values in Table 4.1. For the remaining targets without dynamical mass measurements, we have estimated the BH mass using the $M_{\rm BH} - \sigma_*$ relationship.

Reliable measurements of $M_{\rm BH}$ require kinematic tracers that originate within the BH SOI (approximated by $r_g \approx GM_{\rm BH}/\sigma_*^2$), wherein the BH dominates the gravitational potential. To

first order, the success of a BH mass measurement depends on how well the observations resolve kinematic behavior within r_g. (Barth et al. 2016b; Boizelle et al. 2019) demonstrated that a BH mass measurement is feasible if a sufficient number of resolution elements span the SOI according to $\xi = (2r_g)/\theta \gtrsim 2$. Figure 4.1 shows the r_g values in both physical and angular units for the ETGs in the CEDAR sample, in addition to ξ values for all observations vs $M_{\rm BH}$. As shown, nearby galaxies with larger BHs are easier to measure. Also shown are potential ξ values for the targets in our sample given a hypothetical 0.1" resolution observation. Observations at higher resolution than 0.1" for ALMA begin to introduce exponentially larger integration times, extended configurations, and more execution blocks. However, the feasibility of BH mass measurements does not solely rely on resolving power. High resolution ALMA observations seeking to resolve deep within the SOI have often revealed the presence of a CO hole, rendering many targets unsuitable for high precision molecular $M_{\rm BH}$ measurements.

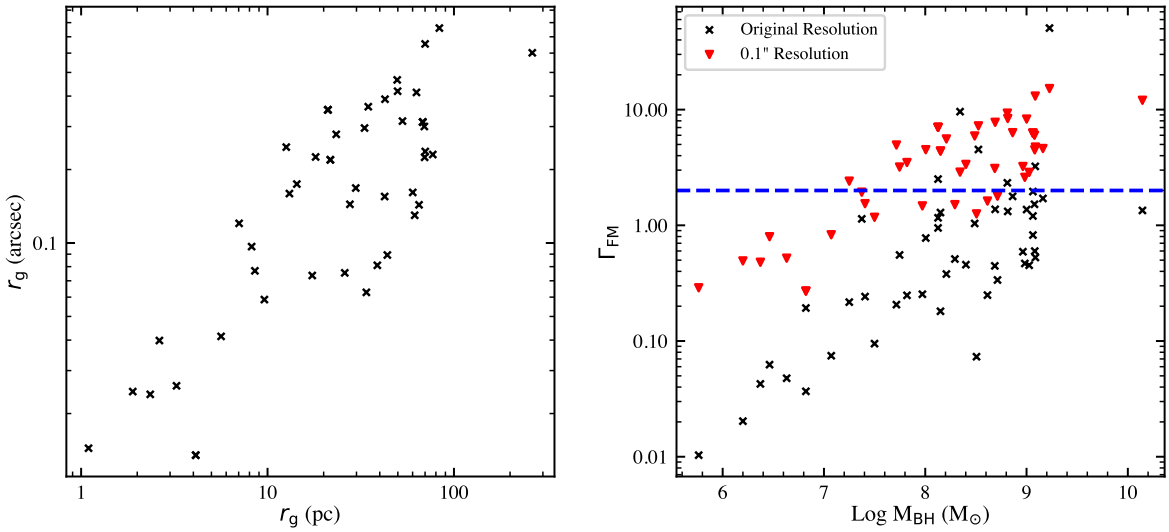

Figure 4.1 Left: Gravitational SOI for SMBHs in the CEDAR sample, shown in both physical and angular units. Right: Supermassive BH masses plotted versus the figure of merit (Γ_{FM}; Davis et al. 2014), wherein a minimum of two resolution elements across the BH SOI are necessary to measure the BH mass using molecular gas kinematics. All targets above the dotted line can potentially demonstrate Keplerian motion due to the BH, at least in the absence of issues such as CO holes or sensitivity limitations. Hypothetical Γ_{FM} values using a standard 0.1" resolution are included, demonstrating that for a significant fraction of the CEDAR sample SMBH mass measurement using molecular kinematics can be possible with 0.1" resolution observations.

Table 4.1. Literature-compiled dynamical black hole masses

Galaxy Name	Log $M_{\rm BH}$	Reference	Dynamical Tracer
IC 1459	9.415	Cappellari 2002	Stars
IC 4296	9.114	Saglia 2016	Stars
NGC 0383	9.623	North 2019	CO
NGC 0524	8.938	Smith 2019	CO
NGC 0612	8.600	Ruffa 2023	CO
NGC 1052	6.630	Onori 2017	X-ray Virial
NGC 1194	7.850	Saglia 2016	Stars
NGC 1326	7.850	Green 2016	Maser
NGC 1332	8.822	Barth 2016	CO
NGC 1380	8.167	Kabasares 2023	CO
NGC 1386	6.070	Smith 2021	Masers
NGC 1399	8.708	Gebhardt 2007	Stars
NGC 1407	9.653	Rusli 2013	Stars
NGC 1453	9.462	Liepold 2020	Stars
NGC 1574	8.000	Ruffa 2023	CO
NGC 1600	10.230	Thomas 2016	Stars
NGC 3081	7.200	Biefiori 2012	Ionized Gas
NGC 3258	9.352	Boizelle 2019	CO
NGC 3377	8.204	Schulze 2011	Stars
NGC 3489	6.778	Nowak 2010	Stars
NGC 3557	8.851	Ruffa 2019	CO
NGC 3607	8.079	Gultekin 2009b	Stars
NGC 3862	8.410	Biefiori 2012	Ionized Gas
NGC 4374	8.966	Walsh 2010	Ionized gas

Table 4.1 (cont'd)

Galaxy Name	Log M_{BH}	Reference	Dynamical Tracer
NGC 4429	8.176	Davis 2018	CO
NGC 4435	6.875	Coccato 2006	Ionized gas
NGC 4594	8.820	Jardel 2011	Stars
NGC 4596	7.892	Sarzi 2001	Ionized gas
NGC 4649	9.653	Shen/Gebhardt 2010	Stars
NGC 4697	8.342	Schulze 2011	Stars
NGC 4742	7.146	Tremain 2002	Stars
NGC 4751	9.146	Rusli 2013	Stars
NGC 5813	8.851	Saglia 2016	Stars
NGC 5846	9.041	Saglia 2016	Stars
NGC 6861	9.301	Rusli 2013	Stars
NGC 7075	8.519	van der Marel 1998	Ionized gas

Note. — Literature compiled dynamical BH measurements for targets in the CEDAR sample.

4.4 Different CO Transitions

Observations in the CEDAR sample consist of CO observations, specifically of low-J rotational transitions 1-0, 2-1, and 3-2. These transitions have rest frequencies of 115.271, 230.538, and 345.796 GHz, respectively. For a select few targets in our sample, archival observations exists of multiple transitions. Observations at different transitions allow for direct comparison of transitions ratios, which serve as diagnostic tool for the thermodynamic conditions of the emitting regions. These CO transitions are typically collisionally excited, with CO(1-0) critical density $n_{crit} \sim 2000$ cm^{-3} needed to populate the $J = 1$ level; for the upper levels, n_{crit} increases to around 10^4 cm^{-3}.

Higher gas temperatures also promote greater occupation of upper rotational states. Thus, CO line ratios serve as a decent probe of cloud H_2 density (n_{H_2}) and excitation energy (kinetic temperature T_K), with an increase in either causing an increase in higher-to-lower line ratios.

Four targets within our sample have multiple CO transitions in the archive, being NGC 3557 and NGC 4697 (1-0 and 2-1 transitions), and NGC 6861 and NGC 4261 (2-1 and 3-2). By re-imaging the spectral cubes such that they have matched resolution and matching spectral axes (in velocity space) direct comparison of the different transitions is possible. It is important to note that the native spectral units for ALMA spectral cubes are frequency units, not velocity units. However, conversion to velocity units can be performed for these cubes to put them into velocity units, typically using the optical velocity convention and the Barycentric reference frame, such that they are aligned spectrally. Figure 4.2 shows the ratio of the different CO transition luminosity (R_{32} for NGC 6861). The overlaid contours match the CO(2-1) emission. Analysis of this ratio map has revealed that R_{32} mostly seems to increase as you get closer to the center of the CND. Possible explanations for this increase could be increasing kinetic temperature, which would be caused by increasing intensity of the stellar radiation field closer to the center of the galaxy, or simply an increase in number density of molecular gas toward the center. Preliminary thermodynamic modeling of these ratios reveal gas temperatures in the 12-30K range for fixed number density (Figure 4.3). These gas temperatures agree with global thermal dust temperatures (Carlisle 2023), suggesting that the gas and the dust are in thermal equilibrium. This work is simply exploratory at this point, and will be continued by future student researchers.

4.5 Conclusion

In this work, I have created the first census of archival ALMA observations of local ETGs. The CEDAR sample furthers the work of previous surveys in analyzing the cold gas properties of ETGs.

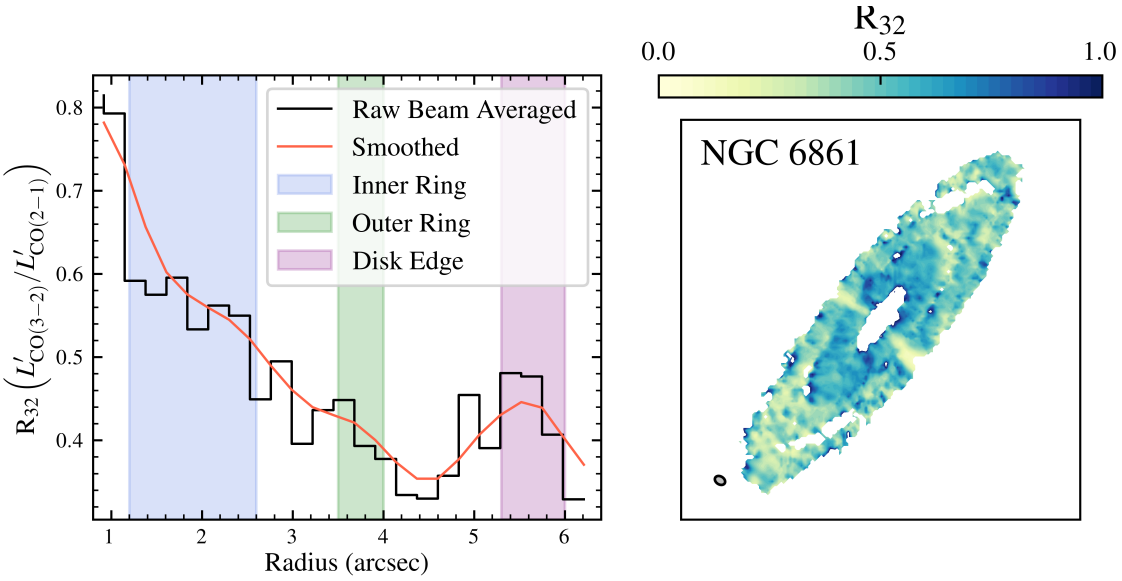

Figure 4.2 Left: Radial R_{32} profile of NGC 6861. Right: Ratio of of flux from the CO 3-2 / 2-1 transitions, with contours overlaid of CO 2-1 flux.

The unparalleled sensitivity and resolution of ALMA allows for detailed studies of disk kinematics and properties. Our final sample exhibited gas masses in the range $10^6 - 10^{10} M_\odot$. We did not find any strong correlations between molecular gas properties and host galaxy properties. We classified CO emission morphology, building on previous work from (Alatalo et al. 2013). We also probed the potential for further BH mass measurement using targets from our sample, and discussed a figure of merit for future observations. Ratios of low J CO transitions shows a slight gradient NGC 6861, revealing higher gas density near the center of the galaxy. Future work will seek to further probe the kinematic properties of the CNDs and constrain thermal dust properties.

A critical question regarding our sample of ETG CNDs is whether the molecular gas is actively forming stars. The existence of a bimodality in galaxy type strongly supports a scenario in which physical processes turn a star-forming blue cloud galaxy into a passive red sequence galaxy, with star formation eventually being quenched. Understanding the star formation rates (or lack thereof) in ETGs would provide further observational evidence on the nature of the quenching mechanism. Many of the proposed quenching channels, such as ram pressure stripping or AGN feedback, cease

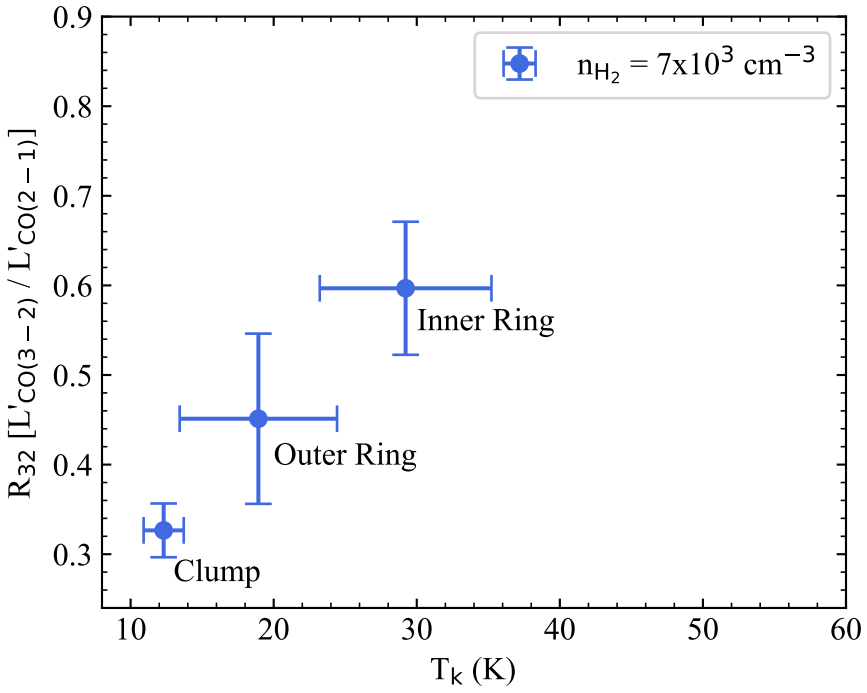

Figure 4.3 Modeling of thermodynamic conditions of the CND of NGC 6861 from the calculated R_{32} values.

star formation by removing molecular gas and starving star formation. However, such mechanisms would likely not be in play should the molecular gas be regenerated in the galaxy. Other quenching mechanisms, such as morphological quenching (Martig et al. 2009; 2013) would render molecular CNDs stable against collapse and thus unable to form new stars. Initial analysis of CND stability using the Toomre local stability parameter found them to be stable against collapse (Boizelle et al. 2017). Further work analyzing the kinematics of these disks will allow us to constrain disk stability.

I note that the CEDAR sample as shown in this thesis is not in its final stage. A forthcoming paper will present the entirety of the CEDAR samples (for ALMA cycles 2-5), expand upon the analysis described here, and provide access to online data products.

Bibliography

Alatalo, K., et al. 2013, MNRAS, 432, 1796

Babyk, I. V., McNamara, B. R., Tamhane, P. D., Nulsen, P. E. J., Russell, H. R., & Edge, A. C. 2019, ApJ, 887, 149

Bacon, R., et al. 2001, MNRAS, 326, 23

Baker, M. K., Davis, T. A., van de Voort, F., & Ruffa, I. 2024, arXiv e-prints, arXiv:2412.03707

Baldry, I. K., Balogh, M. L., Bower, R. G., Glazebrook, K., Nichol, R. C., Bamford, S. P., & Budavari, T. 2006, MNRAS, 373, 469

Baldry, I. K., Glazebrook, K., Brinkmann, J., Ivezić, Ž., Lupton, R. H., Nichol, R. C., & Szalay, A. S. 2004, ApJ, 600, 681

Bamford, S. P., et al. 2009, MNRAS, 393, 1324

Baron, D., et al. 2024, ApJ, 968, 24

Barth, A. J., Boizelle, B. D., Darling, J., Baker, A. J., Buote, D. A., Ho, L. C., & Walsh, J. L. 2016a, ApJ, 822, L28

Barth, A. J., Darling, J., Baker, A. J., Boizelle, B. D., Buote, D. A., Ho, L. C., & Walsh, J. L. 2016b, ApJ, 823, 51

Blakeslee, J. P., Jensen, J. B., Ma, C.-P., Milne, P. A., & Greene, J. E. 2021, ApJ, 911, 65

Boizelle, B. D., Barth, A. J., Darling, J., Baker, A. J., Buote, D. A., Ho, L. C., & Walsh, J. L. 2017, ApJ, 845, 170

Boizelle, B. D., Barth, A. J., Walsh, J. L., Buote, D. A., Baker, A. J., Darling, J., & Ho, L. C. 2019, ApJ, 881, 10

Boizelle, B. D., et al. 2021, ApJ, 908, 19

Bolatto, A. D., Wolfire, M., & Leroy, A. K. 2013, ARA&A, 51, 207

Braine, J., Henkel, C., & Wiklind, T. 1997, A&A, 321, 765

Briggs, D. S. 1995, in American Astronomical Society Meeting Abstracts, Vol. 187, American Astronomical Society Meeting Abstracts, 112.02

Bryant, J. J., et al. 2019, MNRAS, 483, 458

Camacho, C. 2024, Ph.D. dissertation

Cappellari, M., & Copin, Y. 2003, MNRAS, 342, 345

Cappellari, M., et al. 2011, MNRAS, 413, 813

Carilli, C. L., & Walter, F. 2013, ARA&A, 51, 105

Carlisle, E. 2023, Ph.D. dissertation

Chiang, I.-D., et al. 2024, ApJ, 964, 18

Cohn, J. H., et al. 2021, ApJ, 919, 77

Comrie, A., et al. 2021, CARTA: The Cube Analysis and Rendering Tool for Astronomy

Davidson, J. R., et al. 2024, ApJ, 972, 127

Davis, T. A., & Bureau, M. 2016, MNRAS, 457, 272

Davis, T. A., Bureau, M., Onishi, K., Cappellari, M., Iguchi, S., & Sarzi, M. 2017, MNRAS, 468, 4675

Davis, T. A., et al. 2011, MNRAS, 417, 882

—. 2014, MNRAS, 444, 3427

—. 2018, MNRAS, 473, 3818

de Vaucouleurs, G. 1959, Handbuch der Physik, 53, 275

de Vaucouleurs, G., de Vaucouleurs, A., Corwin, Herold G., J., Buta, R. J., Paturel, G., & Fouque, P. 1991, Third Reference Catalogue of Bright Galaxies

Derieg, B. 2024, Ph.D. dissertation

di Serego Alighieri, S., et al. 2007, A&A, 474, 851

—. 2013, A&A, 552, A8

Emsellem, E., et al. 2011, MNRAS, 414, 888

Ene, I., et al. 2018, MNRAS, 479, 2810

Ferrarese, L., & Merritt, D. 2000, ApJ, 539, L9

Fomalont, E., et al. 2014, The Messenger, 155, 19

Franco, M., et al. 2018, A&A, 620, A152

Fujimoto, S., et al. 2023, arXiv e-prints, arXiv:2303.01658

Ganguly, S., et al. 2023, Frontiers in Astronomy and Space Sciences, 10, 1138613

Gebhardt, K., et al. 2000, ApJ, 539, L13

Grogin, N. A., et al. 2011, ApJS, 197, 35

Habe, A., & Ikeuchi, S. 1988, ApJ, 326, 84

Heiderman, A., Evans, II, N. J., Allen, L. E., Huard, T., & Heyer, M. 2010, ApJ, 723, 1019

Ho, L. C., Filippenko, A. V., & Sargent, W. L. W. 1997, ApJ, 487, 568

Hubble, E. P. 1926, ApJ, 64, 321

Izumi, T., Kawakatu, N., & Kohno, K. 2016, ApJ, 827, 81

Izumi, T., et al. 2013, PASJ, 65, 100

—. 2015, ApJ, 811, 39

Jiang, B., Ciotti, L., Gan, Z., & Ostriker, J. 2022, arXiv e-prints, arXiv:2208.03735

Jiménez-Donaire, M. J., et al. 2019, ApJ, 880, 127

Johnson, D. W., & Gottesman, S. T. 1979, in Photometry, Kinematics and Dynamics of Galaxies, ed. D. S. Evans, 57

Jones, J. 2023, Ph.D. dissertation

Kabasares, K. M., et al. 2022, ApJ, 934, 162

Kauffmann, J., Goldsmith, P. F., Melnick, G., Tolls, V., Guzman, A., & Menten, K. M. 2017, A&A, 605, L5

Kennicutt, Robert C., J. 1998, ARA&A, 36, 189

Kenworthy, W. D., et al. 2022, ApJ, 935, 83

Khim, D. J., Yi, S. K., Pichon, C., Dubois, Y., Devriendt, J., Choi, H., Bryant, J. J., & Croom, S. M. 2021, ApJS, 254, 27

Knapp, G. R., Guhathakurta, P., Kim, D.-W., & Jura, M. A. 1989, ApJS, 70, 329

Knapp, G. R., & Rupen, M. P. 1996, ApJ, 460, 271

Kokusho, T., et al. 2019, A&A, 622, A87

Kormendy, J., & Ho, L. C. 2013, ARA&A, 51, 511

Kormendy, J., & Richstone, D. 1995, ARA&A, 33, 581

Krajnović, D., Cappellari, M., de Zeeuw, P. T., & Copin, Y. 2006, MNRAS, 366, 787

Krajnović, D., et al. 2011, MNRAS, 414, 2923

Lada, C. J., Forbrich, J., Lombardi, M., & Alves, J. F. 2012, ApJ, 745, 190

Lagos, C. d. P., Davis, T. A., Lacey, C. G., Zwaan, M. A., Baugh, C. M., Gonzalez-Perez, V., & Padilla, N. D. 2014, MNRAS, 443, 1002

Lauer, T. R., et al. 2005, AJ, 129, 2138

Le Fèvre, O., et al. 2020, A&A, 643, A1

Leroy, A. K., et al. 2021, ApJS, 257, 43

—. 2022, ApJ, 927, 149

Makarov, D., Prugniel, P., Terekhova, N., Courtois, H., & Vauglin, I. 2014, A&A, 570, A13

Martig, M., Bournaud, F., Teyssier, R., & Dekel, A. 2009, ApJ, 707, 250

Martig, M., et al. 2013, MNRAS, 432, 1914

McGuire, B. A. 2018, ApJS, 239, 17

McMullin, J. P., Waters, B., Schiebel, D., Young, W., & Golap, K. 2007, in Astronomical Society of the Pacific Conference Series, Vol. 376, Astronomical Data Analysis Software and Systems XVI, ed. R. A. Shaw, F. Hill, & D. J. Bell, 127

Mould, J. R., et al. 2000, ApJ, 529, 786

Nguyen, D. D., et al. 2020, ApJ, 892, 68

North, E. V., et al. 2019, MNRAS, 490, 319

Nyland, K., et al. 2016, MNRAS, 458, 2221

Olivares, V., et al. 2019, A&A, 631, A22

Riess, A. G., et al. 2022, ApJ, 934, L7

Ruffa, I., et al. 2019, MNRAS, 484, 4239

—. 2023, MNRAS, 522, 6170

Sage, L. J., & Wrobel, J. M. 1989, ApJ, 344, 204

Saglia, R. P., et al. 2016, ApJ, 818, 47

Saintonge, A., & Catinella, B. 2022, ARA&A, 60, 319

Sandage, A. 1961, The Hubble Atlas of Galaxies

Sandstrom, K. M., et al. 2013, ApJ, 777, 5

Schawinski, K., Thomas, D., Sarzi, M., Maraston, C., Kaviraj, S., Joo, S.-J., Yi, S. K., & Silk, J. 2007a, MNRAS, 382, 1415

Schawinski, K., et al. 2007b, ApJS, 173, 512

Serra, P., et al. 2012, MNRAS, 422, 1835

Smith, M. D., et al. 2019, MNRAS, 485, 4359

Smith, M. W. L., et al. 2012, ApJ, 748, 123

Teague, R., & Foreman-Mackey, D. 2018, Research Notes of the American Astronomical Society, 2, 173

Teng, Y.-H., et al. 2023, ApJ, 950, 119

Tran, H. D., Tsvetanov, Z., Ford, H. C., Davies, J., Jaffe, W., van den Bosch, F. C., & Rest, A. 2001, AJ, 121, 2928

van de Voort, F., Davis, T. A., Kereš, D., Quataert, E., Faucher-Giguère, C.-A., & Hopkins, P. F. 2015, MNRAS, 451, 3269

Walter, F., et al. 2016, ApJ, 833, 67

Wiklind, T., & Henkel, C. 1989, A&A, 225, 1

Wright, E. L. 2006, PASP, 118, 1711

York, D. G., et al. 2000, AJ, 120, 1579

Young, L. M., et al. 2011, MNRAS, 414, 940

—. 2014, MNRAS, 444, 3408

Zhang, H., et al. 2025, arXiv e-prints, arXiv:2501.06303

Index

Active Galactic Nuclei, 3

Carbon monoxide, 3

Early type galaxies, 1

Interstellar Medium, 2

Late type galaxies, 1

Molecular Gas, 2

Supermassive Black Holes, 3